Particle image velocimetry in a centrifugal pump: details of the fluid flow at different operation conditions

Rodolfo M. Perissinotto*[a], Rafael F. L. Cerqueira*[b], William D. P. Fonseca[a], William Monte Verde[b], Jorge L. Biazussi[b], Antonio Carlos Bannwart[a], Erick M. Franklin[a], Marcelo S. Castro[a,b]

[a]School of Mechanical Engineering, University of Campinas, R. Mendeleyev, 200, Campinas-SP, Brazil
[b]Center for Energy and Petroleum Studies, University of Campinas, R. Cora Coralina, 350, Campinas-SP, Brazil

Abstract

Centrifugal pumps are present in the daily life of human beings. They are essential to several industrial processes that transport single- and multi-phase flows with the presence of water, gases, and emulsions, for example. When pumping low-viscous liquids, the flow behavior in impellers and diffusers may affect the centrifugal pump performance. For these flows, complex structures promote instabilities and inefficiencies that may represent a waste of energetic and financial resources. In this context, this paper aims at characterizing single-phase water flows in one complete stage of a centrifugal pump to improve our understanding of the relationship between flow behavior and pump performance. For that, a transparent pump prototype was designed, manufactured and installed in a test facility, and experiments using particle image velocimetry (PIV) were conducted at different conditions. The acquired images were then processed to obtain instantaneous flow fields, from which the flow characteristics were determined. Our results indicate that the flow morphology depends on the rotational speed of the impeller and water flow rate: (i) the flow is uniform when the pump works at the best efficiency point (BEP), with streamlines aligned with the blades, and low vorticity and turbulence in the impeller; (ii) the velocity field becomes complex as the pump begins to operate at off-design conditions, away from BEP. In this case, velocity fluctuations and energy losses due to turbulence increase to higher numbers. Those results bring new insights into the problem, helping validate numerical simulations, propose mathematical models, and improve the design of new impellers.

Keywords: Centrifugal pump, single-phase flow, particle image velocimetry

---

*Corresponding author: Rodolfo M. Perissinotto (rodolfomp@fem.unicamp.br)

1. Introduction

Pumps are devices used by mankind for nearly 3000 years to add energy to and transport liquids, historical records suggesting that African, Asian, Babylonian and Roman civilizations have been using pumps since the year 1000 B.C. [1]. Nowadays, centrifugal pumps are used in a wide range of industrial processes. It is estimated that they are responsible, directly or indirectly, for 20% of the global demand of electricity [2]. In this way, centrifugal pumps are highly relevant to the oil industry, where they usually belong to a type of artificial lift system named electrical submersible pump (ESP). It was estimated that ESP systems were installed in more than 150,000 wells [3] that produced approximately 10% of the world's oil [4] over the last years. These numbers reveal the importance of centrifugal pumps for energy production and human activities in general.

Centrifugal pumps were originally designed to operate with incompressible and low-viscous fluids. However, when working in oil wells, these pumps often handle two-phase or even three-phase mixtures, organized in different patterns. The presence of free gas occurs below the saturation point, while oil-water or water-oil emulsions are formed due to the connate water from the reservoir rock [5]. When the pump transports multiphase flows, it undergoes operational issues, such as instabilities and performance reduction [6], conditions which may lead to lower production, shorter pump lifetime, and more frequent well interventions.

As the pump behavior is a consequence of the flow in its impellers and diffusers, many researchers worldwide have used visualization methods to study the characteristics of single- and two-phase flows within these turbomachines. According to Perissinotto et al. [7], the technological improvement of computers, digital cameras, and laser generators has engendered the popularization of non-intrusive techniques for flow visualization, such as the high-speed imaging (HSI), particle tracking velocimetry (PTV), particle image velocimetry (PIV), and laser Doppler velocimetry (LDV) [8, 9].

With regard to two-phase flows, HSI and PTV methods were used for flow visualization in pumps, such as Gamboa and Prado [10], Trevisan and Prado [11], Monte Verde et al. [12], Shao et al. [13], and Zhao et al. [14], who observed gas-liquid patterns and studied the surging and gas-locking phenomena, while the bubble dynamics was addressed by Stel et al. [15] and Cubas et al. [16]. The visualization of liquid-liquid dispersions in impellers was performed by Perissinotto et al. [17, 18] with a HSI method and a PTV approach was afterward carried out by Cerqueira et al. [19] to analyze the dynamics of oil drops and water drops. Other researchers visualized emulsions

2

upstream or downstream of pumps by using endoscopes and microscopes [20, 21] to measure the characteristic length of dispersed drops. Phenomena such as phase inversion and effective viscosity were investigated by Bulgarelli et al. [22, 23, 24].

Furthermore, the PIV technique has been used for about three decades to investigate single-phase flows in pumps, the method becoming more accessible over time. Among the most recent and relevant studies, we can cite Pedersen et al. [25], Keller et al. [26], Zhang et al. [27], Li et al. [28], Shi et al. [29], Liu et al. [30], and Chen et al. [31], who used two-dimensional PIV with Nd:YAG lasers in frequencies up to 100 Hz in order to obtain results such as average velocity fields, streamlines, vorticity, and turbulent kinetic energy. Fewer authors (e.g. Krause et al. [32]) preferred to operate the lasers at higher frequencies, and others (e.g. Mittag and Gabi [33]) used mineral oil instead of water.

The centrifugal pumps used in those studies were made of transparent components, allowing visual access to their radial impellers. In general, these pumps worked at rotational speeds in the range within 500 to 1000 rpm, and at various flow rates corresponding to different percentages of the best efficiency point (BEP). However, the development of transparent pumps and execution of PIV tests are complex activities, so that most works available in the literature have their measurements limited to small regions of the pump impellers. Therefore, the behavior of single-phase flows is still an open question and the investigation of single-phase flows remains necessary. For example, the visualization of all channels of the impeller and the diffuser, simultaneously, is missing.

In this context, the present paper aims at improving the comprehension of the single-phase water flow in a centrifugal pump. To achieve this target, a new test facility was assembled and a transparent pump was designed and manufactured. An experimental program was then carefully conducted using a time-resolved PIV system, fluorescent tracer particles, and a robust and reliable instrumentation. Routines in Python$^{\text{TM}}$ and MATLAB$^{\circledR}$ were developed in the course of this work to process the PIV images and provide the desirable results. Our results indicate that the flow morphology depends on the rotational speed of the impeller and water flow rate: (i) the flow is uniform when the pump works at the best efficiency point (BEP), with streamlines aligned with the blades, and low vorticity and turbulence in the impeller; (ii) the velocity field becomes complex as the pump begins to operate at off-design conditions, away from the BEP. In this case, velocity fluctuations and energy losses due to turbulence increase to higher numbers. Those results bring new insights into the problem. They may help validate numerical simulations, propose mathematical models, improve the design of new impellers, among other applications.

In the following, we present the experimental setup in Sec. 2, the results in Sec. 3, and the conclusions in Sec. 4.

2. Experimental program

The experimental program adopted in this paper is minutely explained in this section. Subsection 2.1 presents the experimental apparatus, Subsection 2.2 contains the test matrix, Subsection 2.3 presents the activities performed to set up the PIV system, and Subsection 2.4 describes the procedures adopted to conduct the experiments and process flow images acquired with the PIV method.

2.1. Test facility and transparent pump prototype

The test facility depicted in Fig. 1 was designed and assembled as described in Perissinotto et al. [34]. As shown in Fig. 1, the facility consists basically of a closed water circuit, a flow visualization system, and a transparent prototype of a centrifugal pump. A booster pump draws water from the tank, then the liquid passes through the Coriolis flowmeter, heat exchanger, pressure and temperature transducers, before reaching the suction point of the transparent pump. Experimental measurements are conducted by using a PIV system installed inside the safety cover. An angular encoder measures the angular position and rotational speed of the rotor of the transparent pump, while the torque meter measures the torque of the pump shaft. Then, the fluid returns to the tank, where the recirculation pump keeps the water mixed with PIV tracers, which are basically solid particles (described next) added to the water. The pumps are driven by variable speed drives that enable the adjustment of the rotational speed, and, as a result, the flow rate control. In addition, control valves help regulating the absolute pressure and the water flow rate in the circuit.

The water mass flow rate ($\dot{m}$) is measured with a Coriolis meter, model F200, series *Micro-Motion*, manufactured by *Emerson*, which has a top limit of 32000 kg/h and an uncertainty of 0.2% of the measured value. In the prototype inlet, the water temperature (T) is measured with a resistance temperature detector, type PT100, with 1/10 DIN accuracy. The gauge pressure (P) and differential pressure (ΔP) between the pump suction and discharge are quantified with capacitive transducers, series 2051 and 2088, manufactured by *Rosemount*, with an uncertainty of 0.05% of the measured value. The rotational speed (N) and angular position (θ) of the impeller are measured with an angular encoder, model RUP500, by *IFM Electronic*, whose uncertainty is less than 0.1%. The torque (τ) is measured with a torque meter installed in the pump shaft,

4

model MT-102 FC, manufactured by *TransTec*, with an uncertainty limited to 0.5%. The analog output signals from these instruments are acquired through a *National Instruments* system and the measured data is monitored and stored via a LabVIEW$^{\text{TM}}$ supervisory control program.
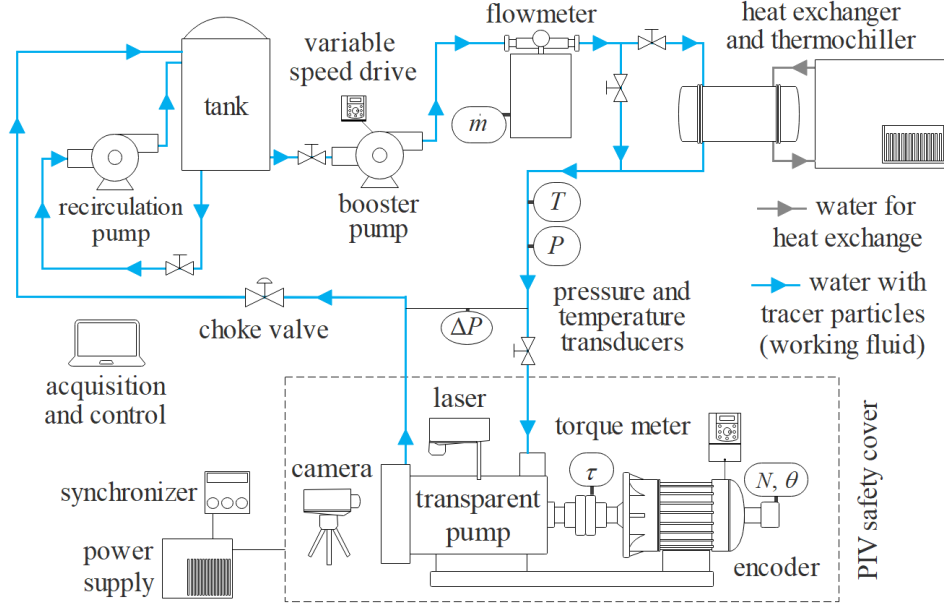

Figure 1: Diagram of the test facility.

The transparent pump installed in the experimental apparatus was designed and manufactured for flow visualization purposes. As mentioned by Perissinotto et al. [34], this pump prototype has components made of acrylic material that provide visual access to the flow within its impeller and vaneless diffuser. The pump impeller has the same geometry as that one used by Monte Verde et al. [12] and Perissinotto et al. [17, 18] to study two-phase flows, i.e., a P23 model, *Centrilift* series, manufactured by *Baker-Hughes*. The impeller has seven transparent blades, a $h = 6$ mm height, $r_o = 55$ mm outer radius, and $r_i = 22$ mm inner radius. The pump stage is presented in Fig. 2.

The visualization section of the new pump prototype basically consists of two flat plates joined by screws and nuts: a black anodized aluminum base and a transparent core with a polished acrylic front cover, where the volute spiral is machined [34]. In addition, the pump has other components, such as a body, a shaft, four intake ports through which the fluid enters, and a discharge port through which the fluid exits the pump. The inlet ports are located at the pump body, while the outlet port is assembled in the end of the volute spiral. The design of the volute spiral has followed
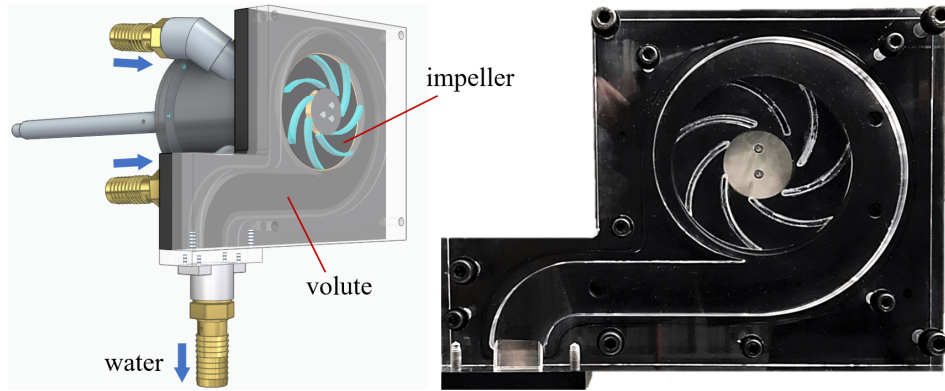
5

Figure 2: Technical drawing (left) and photograph (right) of the centrifugal pump prototype.

the guidelines recommended by Stepanoff [35] and Petermann and Pfleiderer [36].

The experimental facility used in this study contains a *DualPower 30-1000* PIV system provided by *Dantec Dynamics*. It consists of a Nd:YAG laser generator, a power supply with cooling system, a high-resolution signal synchronizer, and a high-speed camera. The system is controlled through the *DynamicStudio 7.4* software. Optical elements such as beam splitters and adjustable mirrors complement the system for the formation of two overlapping laser planes, emitted in opposite directions, that enter the prototype from both sides and then illuminate the entire stage. These components are assembled inside a safety cover together with the transparent pump and laser head. The photographs available in Fig. 3 show the test facility during a PIV experiment.
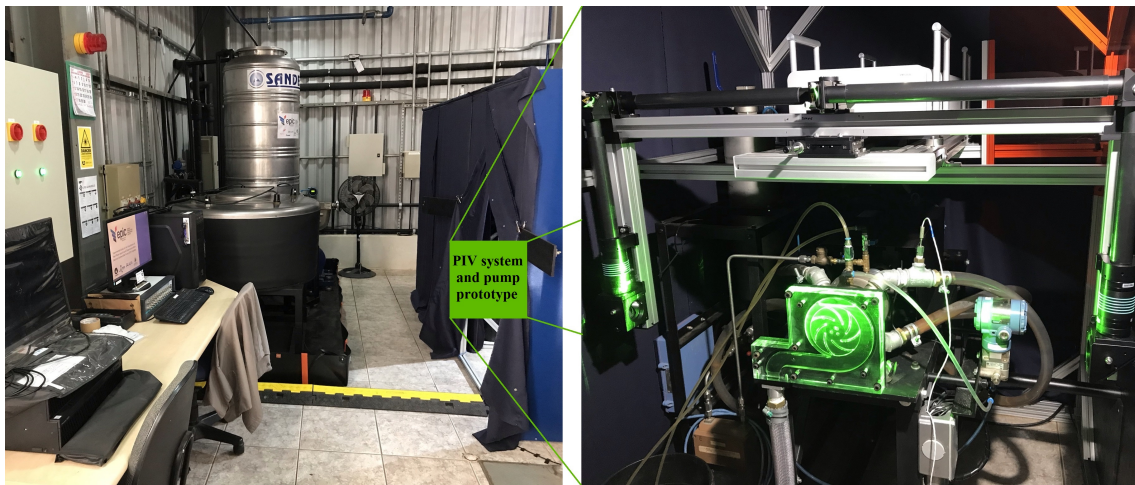

Figure 3: Test facility (left) with zoom on transparent pump and flow visualization system (right).

Table 1: Test matrix with 12 operating conditions.

| N | $\dot{m}$ - absolute and relative to $\dot{m}_{BEP}$ | | | | | |
	~10%	~30%	~80%	~100%	~120%	~160%
600 rpm	150 kg/h	450 kg/h	1200 kg/h	1500 kg/h	1800 kg/h	2400 kg/h
900 rpm	150 kg/h	750 kg/h	1800 kg/h	2200 kg/h	2600 kg/h	3600 kg/h

2.2. Test matrix and pump performance

The experimental matrix for the present study contains 12 operational conditions investigated with PIV, as listed in Tab. 1, with two impeller rotational speeds and various water flow rates.

The conditions include rotational speeds of $N = [600, 900]$ rpm and ten flow rates in the range $150 \leq \dot{m} \leq 3600$ kg/h. These flow rates, when referenced as percentages of the best efficiency point (BEP), are equivalent to flow rates that vary from 10% to 160% of $\dot{m}_{BEP}$, approximately. The Coriolis flow meter measures these mass flow rates, but they can be converted into volumetric flow rates by being divided by the water density, i.e., $Q = \dot{m}/\rho$. During the tests, the water was at a constant temperature of $T = 25°C$, thus the fluid density was assumed $\rho = 997$ kg/m³. In addition, at this temperature the viscosity was assumed $\mu = 0.0009$ Pa.s.

The rotations were limited due to concerns with the integrity of the polymeric parts that compose the pump prototype. At values higher than 1000 rpm, the pressure at the pump inlet reached $P = 200$ kPa, a value classified as the limit for a safe operation. In this sense, the rotational speeds were restricted to a maximum of $N = 900$ rpm, in order to preserve the most delicate elements of the centrifugal pump, such as the impeller, made of thin parts.

Furthermore, the flow rates defined in the test matrix were obtained through preliminary tests that characterized the pump performance. The pump efficiency was firstly calculated from the quantities measured by the instruments. The flow rate corresponding to the BEP ($\dot{m}_{BEP}$) was then determined for both rotations. As displayed in Fig. 4, the flow rates analyzed in this paper range from a condition close to shut-off (highest pump head and lowest flow rate) to a condition close to open-flow (lowest pump head and highest flow rate). In Fig. 4, the dimensionless head (Ψ), dimensionless flow rate (Φ), and efficiency (η) are defined as [6]:

$$\Psi = \frac{gH}{\Omega^2 D^2} \quad , \quad \Phi = \frac{Q}{\Omega D^3} \quad \text{and} \quad \eta = \frac{\rho g H Q}{\Omega \tau} \tag{1}$$

where g is the modulus of the gravitational acceleration in m/s²; $H = \Delta P/\rho g$ is the pump head

7

in m, which depends on the differencial pressure (ΔP) and water density (ρ); $\Omega = \pi N/30$ is the angular speed in rad/s, proportional to the impeller rotational speed (N); $D = 2r_o$ is the impeller diameter in m, proportional to the outer radius (r_o); Q is the volumetric water flow rate in m^3/s; τ is the torque at the pump shaft in N.m.
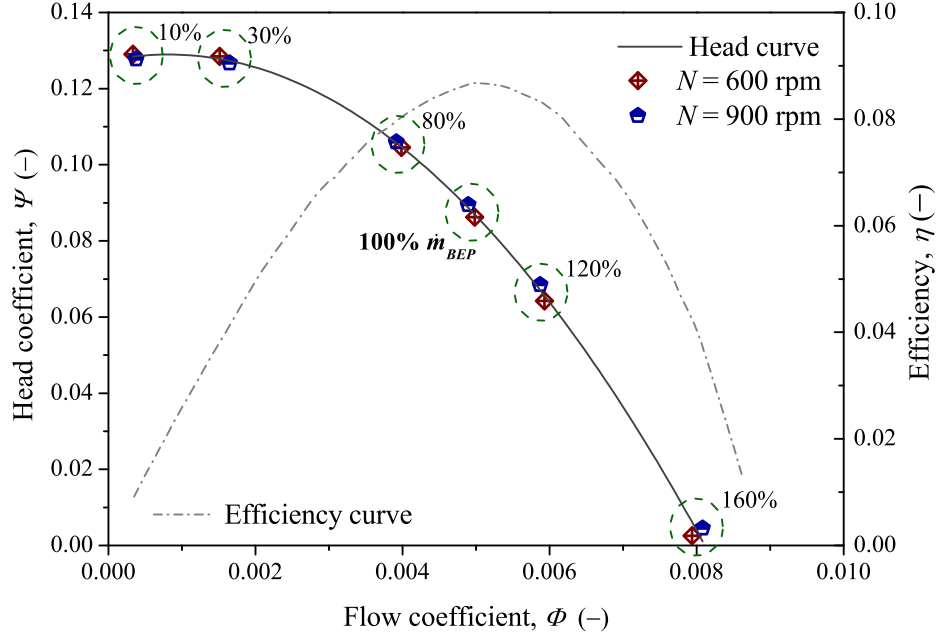

Figure 4: Performance curve in dimensionless form, with the experimental conditions studied in this paper.

Therefore, when operating at $N = 900$ rpm and $\dot{m}_{BEP} = 2200$ kg/h, the transparent pump provides $\Delta P = 9.9$ kPa, i.e., $H = 1.0$ m. The efficiency is $\eta_{BEP} = 8.8$ %, a very low value when compared to the efficiency of commercial pumps. The reason for the reduced η lies in the energy losses that occur in the mechanical components located in the transmission system that connects the electric motor to the pump impeller. In fact, the motor-pump set has five bearings and three mechanical seals that dissipate energy due to friction, and the torque meter measures the total torque necessary to move all these elements. The length of the central shaft (≈ 80 cm) is almost eight times greater than the diameter of the impeller (≈ 10 cm).

However, it is important to emphasize that the low efficiency of the prototype is not an obstacle for this study, as this pump was designed for flow visualization purposes. The inclusion of bearings and seals on the shaft reduced the efficiency, but did not compromise the functioning of the machine,

which provided head curves consistent with a real centrifugal pump. Furthermore, the efficiency rises to $\eta_{BEP} \approx 60$ % when the power consumed by the mechanical elements is subtracted from the total power consumed by the pump. To estimate this dissipated power, another test was carried out: the torque was measured when the pump was "dry running", that is, operating without any liquid inside.

2.3. Activities to configure the PIV system

As stated in Subsection 2.1, a PIV system was used as the flow visualization method for the measurement of velocities and other quantities within the centrifugal pump stage. The PIV equipment is classified as time-resolved (TR-PIV) since it is able to operate at 1 kHz repetition rate while providing a maximum energy of 30 mJ per pulse. In the present study, however, the laser was set to work at a 200 Hz rate only. This repetition frequency was sufficient to perform the necessary acquisitions, which were focused on ensemble-averaged instead of instantaneous results.

Before starting the tests, the position, inclination, and thickness of the laser planes were adjusted for an uniform illumination of the pump stage. The planes were thus positioned perpendicularly to the camera lens, in a configuration that illuminated the entire pump stage (x and y direction) in the central region of the impeller height (z direction), according to Fig. 5. As the laser sheets had their thickness set to approximately 1.0 mm, they entered the impeller 2.5 mm away from the impeller top (shroud) and bottom (hub) covers.

The preparation activities then advanced to the choice of suitable seeding particles. This task consisted of adding a small amount of water with particles into the visualization section of the centrifugal pump, and then acquiring and analyzing a few PIV images to define which tracer provided the most satisfactory images. Hollow glass microspheres and polyamide particles produced improper images full of shadows and regions with excess light, while acrylic particles doped with rhodamine-B dye yielded better flow images with homogeneously distributed illumination, as can be seen in Fig. 6.

Thus, the particles doped with rhodamine-B were used as tracers in the PIV tests defined in Subsection 2.2. In the scope of laser-induced fluorescence (LIF-PIV), the rhodamine-B dye emit an orange light when it is excited by the green laser sheet. A high band-pass filter for wave lengths above 545 nm is then mounted in front of the camera lens, so the camera sensor detects only the light scattered by the seeding particles, in a practice that avoids undesirable reflections from the blades and other pump parts. The fluorescent particles used in this paper have an average diameter
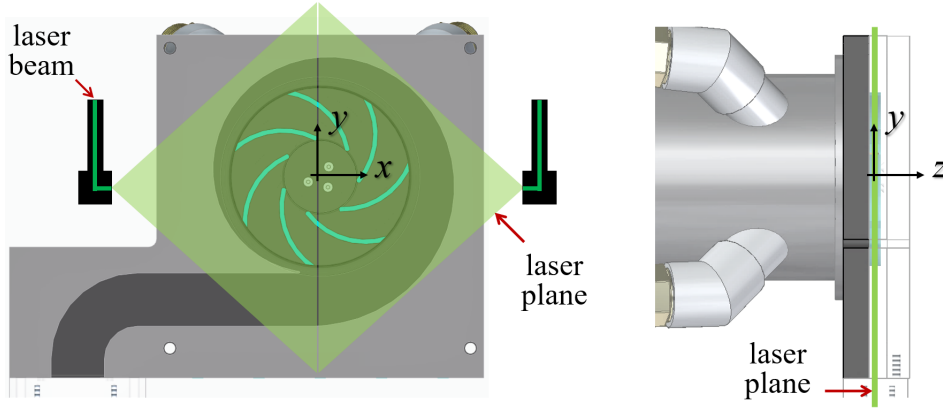
9

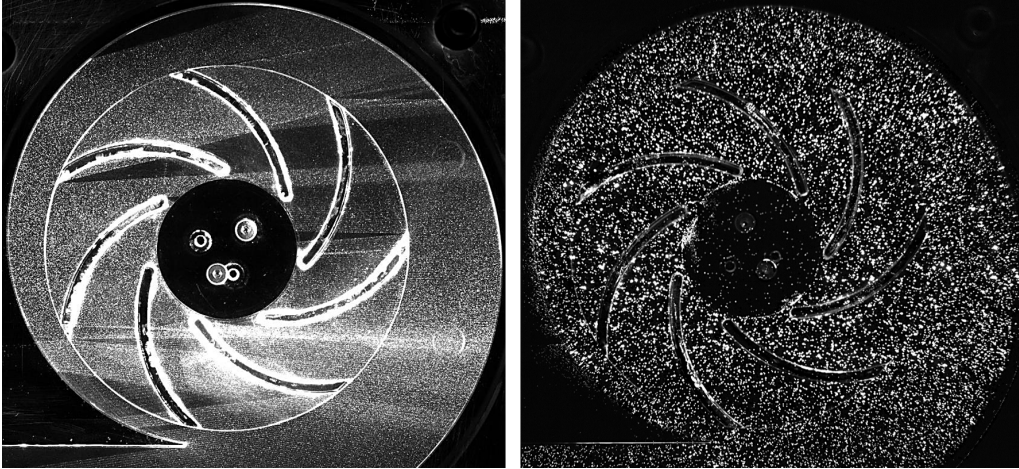Figure 5: Illustration of the laser plane configuration in x, y, and z directions.

Figure 6: PIV images after the addition of common microspheres (left) and fluorescent particles (right).

of 50 μm whose reflected light corresponds to approximately 5 pixels on the flow images.

The images captured by the camera have a dimension up to 2560×1600 pixels when the device operates at acquisition rates below 1400 fps. For the PIV tests executed in this paper, a lens with a focal length of 50 mm was mounted on the camera, and the pump stage was positioned in the center of the camera's field-of-view. By knowing the image dimension and the impeller diameter, a calibration was conducted to specify the conversion factor between image elements and length units. Therefore, it was determined that 10 pixels (image) correspond to 1 millimeter (object).

The definition of the time interval (δt) between two consecutive laser pulses was the last activity accomplished to set up the PIV system. This task demanded the execution of PIV tests exclusively

10

to find the adequate δt for each condition listed in Tab. 1. Satisfactory results were obtained with $300 \leq \delta t \leq 800 \ \mu s$, which limited the maximum displacement of the tracer particles to 10 pixels between consecutive frames. As claimed by Raffel et al. [8], there is an optimal value for this interval: If δt is too small, there is an increment in the velocity uncertainty, which is inversely proportional to time; However, if δt is too large, there is an increase in the displacement uncertainty due to sampling errors and particle losses between the images.

2.4. Procedure to acquire and process flow images

The PIV experiments consist of capturing 500 pairs of flow images at each operational condition presented in Tab. 1. To ensure that the average velocity fields are properly computed, the acquisitions are performed only when the impeller reaches a certain angular position (θ) during its rotational motion. Therefore, when looking at the images, the observer realizes that the channels and blades are always at the same position. In this paper, the PIV tests were carried out at three different angles: $\theta = [0°, 10°, 30°]$, the $0°$ reference position corresponding to the angle at which the tip of one of the lowest impeller blades is vertically aligned with the tip of the volute tongue. The periodicity of the impeller geometry motivated the choice to take measurements at these positions. As the impeller has seven channels, its geometry is repeated every $360°/7 = 51.4°$, or $50°$, approximately.

After completing each experiment, the acquired images are processed in the *DynamicStudio 7.4* software, where filters are firstly applied to the raw images to improve their quality. Then, an algorithm coded in MATLAB$^®$ masks out the impeller blades and regions outside the pump stage where the fluid is not present, while another algorithm based on the work by Liu et al. [30] removes the angular displacement of the impeller between consecutive pulses. This strategy is equivalent to defining a non-inertial frame of reference that rotates together with the impeller. The cross-correlation method is then applied to the images, in an adaptative PIV approach as reported by Scarano and Riethmuller [37]. The present paper uses initial and final interrogation regions of 64×64 and 32×32 pixels, respectively, and a Gaussian fit through the correlation peak to accurately compute sub-pixel displacements.

After concluding the steps described above, the result is a set of 500 instantaneous fields of relative velocities (relative to the blades), which are finally converted into single fields of ensemble-averaged relative velocities and second order moments. Routines developed in Python^{TM} complement the procedure with the calculation of absolute velocities and derived quantities, such as

vorticity and turbulent kinetic energy, which are interpolated to provide smooth graphs and contour plots. The diagram depicted in Fig. 7 summarizes the image processing methodology. Results are presented and discussed in the next section.
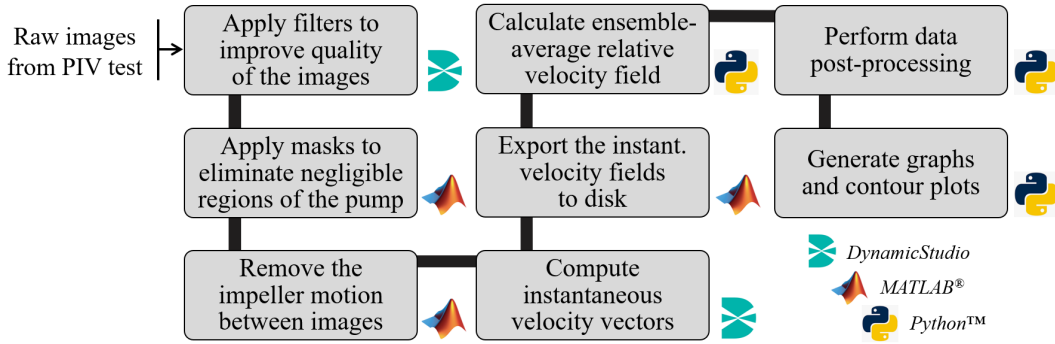

Figure 7: Diagram with the methodology adopted to process the PIV images.

3. Results and discussions

The main results obtained from acquiring and processing PIV images are presented in the next paragraphs. Subsection 3.1 begins the analysis by describing the relative velocity fields measured in the impeller at the angular position $\theta = 0°$.

3.1. Relative velocity fields in the impeller

The ensemble-average relative velocity ($\vec{u}$) fields for the 12 conditions listed in Tab. 1 are presented in Fig. 8 for $N = 600$ rpm and Fig. 9 for $N = 900$ rpm. The impeller rotates in the clockwise direction.

In Figs. 8a and 9a, with flow rates corresponding to $\dot{m} = 0.1\ \dot{m}_{BEP}$, it is possible to observe that the relative velocity is very low in a large part of the impeller. The highest velocities are found only in the channels of the first quadrant. Conversely, the channels of the second and third quadrants have a more complex flow, with vortices that rotate clockwise and counterclockwise, similar to those visualized by Pedersen et al. [25] and Krause et al. [32]. Similar flow structures are identified when the pump operates at $\dot{m} = 0.3\ \dot{m}_{BEP}$, a condition shown in Figs. 8b and 9b.

At $\dot{m} = 0.8\ \dot{m}_{BEP}$, the vortices are extincted and the flow becomes more uniform, as noticed from Figs. 8c and 9c. At this point, the fluid velocity is lower on the suction blades of the second quadrant. Then, Figs. 8d and 9d contain $\vec{u}$ for $\dot{m} = 1.0\ \dot{m}_{BEP}$. We observe that the flow field
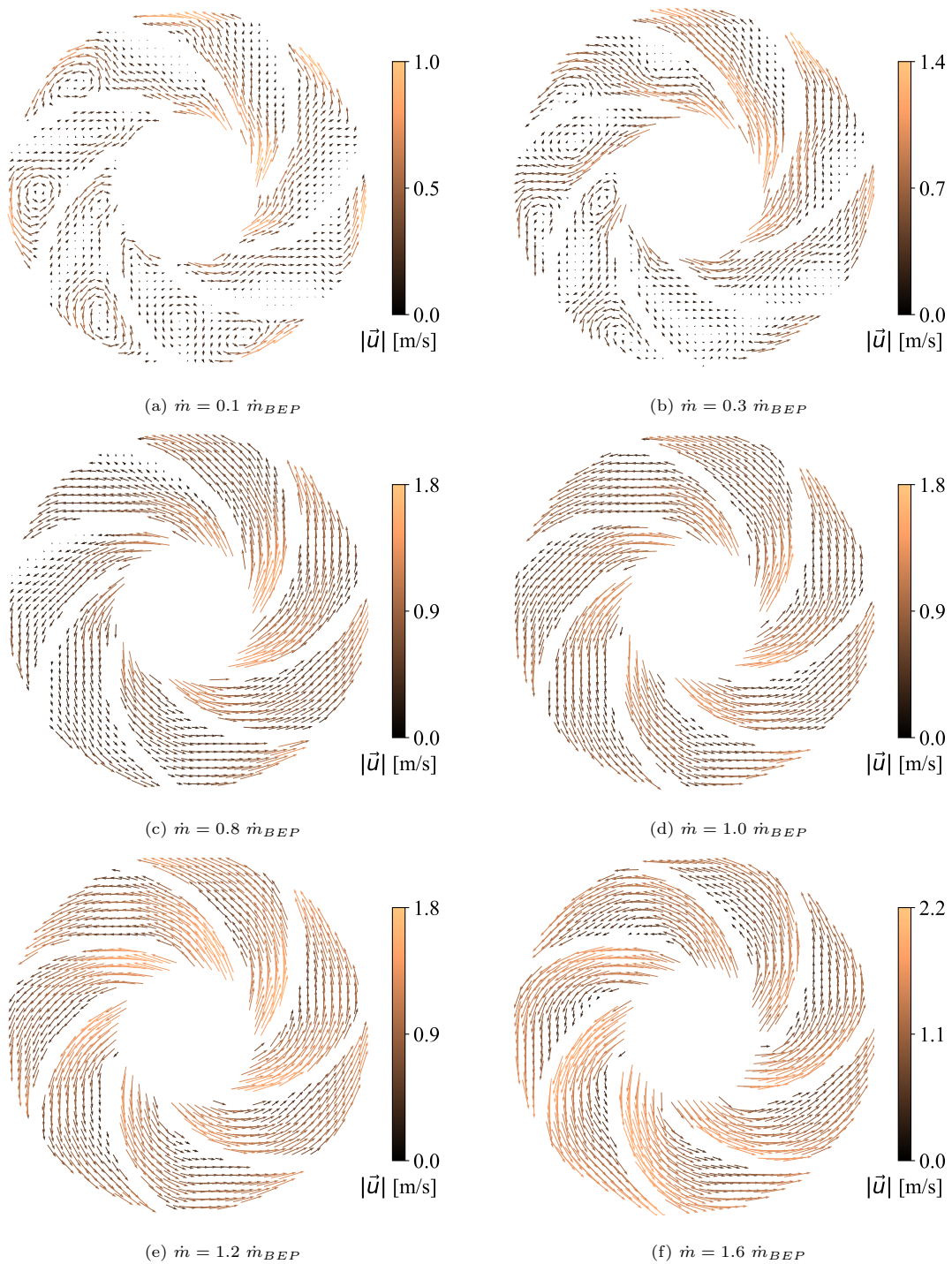
12

(a) $\dot{m} = 0.1 \, \dot{m}_{BEP}$

(b) $\dot{m} = 0.3 \, \dot{m}_{BEP}$

(c) $\dot{m} = 0.8 \, \dot{m}_{BEP}$

(d) $\dot{m} = 1.0 \, \dot{m}_{BEP}$

(e) $\dot{m} = 1.2 \, \dot{m}_{BEP}$

(f) $\dot{m} = 1.6 \, \dot{m}_{BEP}$

Figure 8: Average relative velocity $\vec{u}$ for $N = 600$ rpm and $\theta = 0°$. Rotating frame of reference.

13

(a) $\dot{m} = 0.1 \; \dot{m}_{BEP}$

(b) $\dot{m} = 0.3 \; \dot{m}_{BEP}$

(c) $\dot{m} = 0.8 \; \dot{m}_{BEP}$

(d) $\dot{m} = 1.0 \; \dot{m}_{BEP}$

(e) $\dot{m} = 1.2 \; \dot{m}_{BEP}$
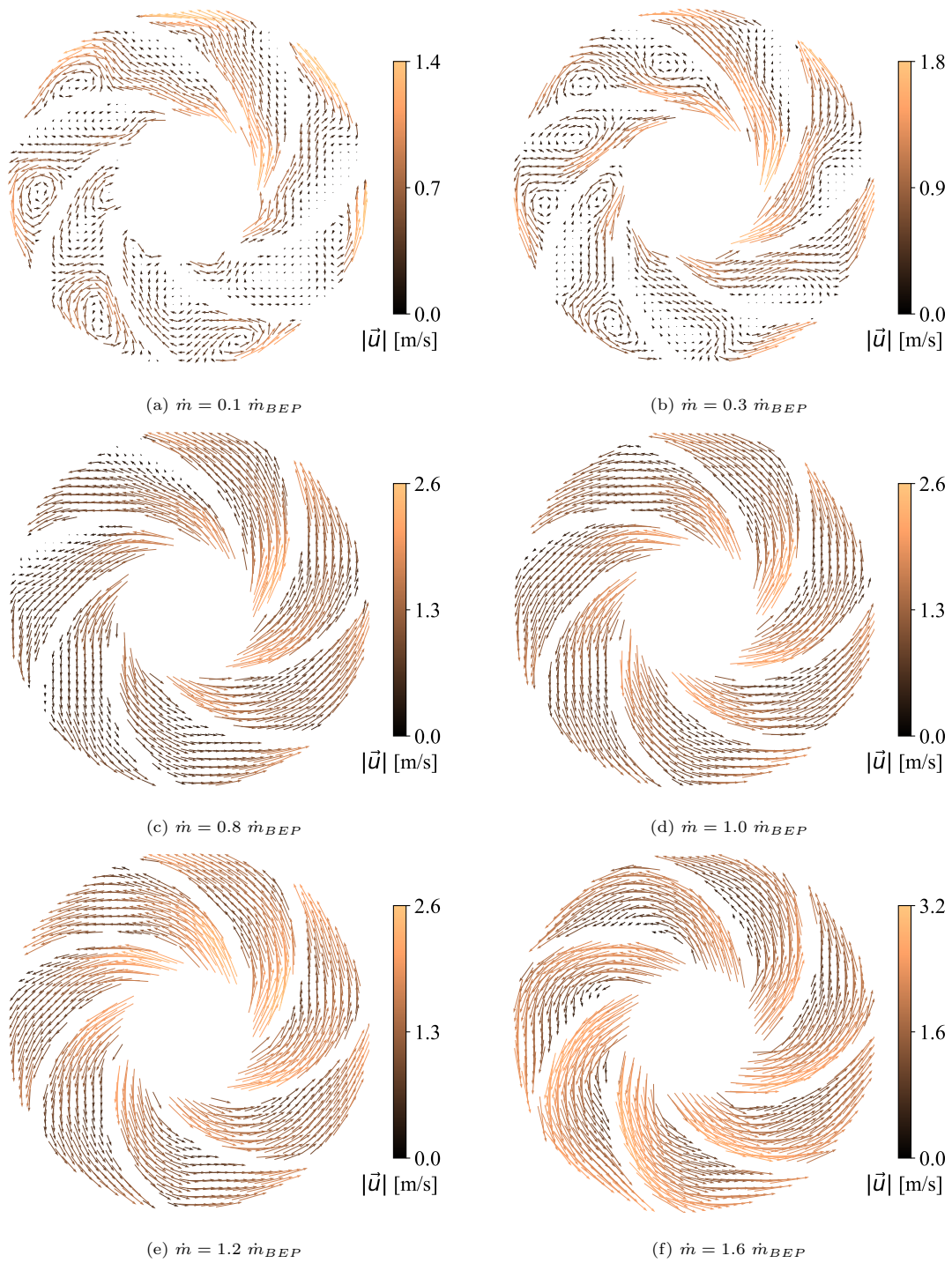
(f) $\dot{m} = 1.6 \; \dot{m}_{BEP}$

Figure 9: Average relative velocity $\vec{u}$ for $N = 900$ rpm and $\theta = 0°$. Rotating frame of reference.

14

is uniformly distributed in the channels and the direction of the vectors is roughly parallel to the curvature of the blades. The energy losses should be minimal in this condition.

The magnitude of the average relative velocity, $|\vec{u}|$, is proportional to the water flow rate, $\dot{m}$. In addition: 1) The velocity is higher at the entrance and lower at the exit of each channel, whose geometry is similar to a divergent nozzle; 2) the velocity is higher in the channels to the right and lower in the channels to the left of the impeller, as a result of the interaction with the solid walls that compose the volute. As depicted in Fig. 2, the volute spiral has its minimum radius in the third quadrant, and its maximum radius in the fourth quadrant of the impeller.

In Figs. 8e and 9e and finally Figs. 8f and 9f, the vectors undergo a gradual deviation. In the first half of the channels, the vectors $\vec{u}$ deviate toward the suction surface of the blades. However, in the second half, they deviate toward the pressure surface. This trend, observed by Keller [38], has three consequences: 1) The fluid path becomes longer; 2) the boundary layer detaches from the pressure blades; 3) the general structure in each channel is similar to half of a large vortex that rotates counterclockwise.

The comparison between Figs. 8 and 9 reveals that, after an increment of 50% in N, the vector magnitude $|\vec{u}|$ increases by a similar proportion. However, the morphology of the flow in the impeller is pretty much the same for both $N = 600$ rpm and $N = 900$ rpm. In fact, the velocity distributions tend to be similar when comparing two different N, as long as both $\dot{m}$ referenced in terms of $\dot{m}_{BEP}$ are identical. This subsection thus evidences the relevant relationship between pump performance and flow morphology. The flow field follows the affinity laws of the centrifugal pump. Thus, for two identical (Φ, Ψ) conditions in Fig. 4, the flow structures will be very similar. This type of analysis that links the flow fields with dimensionless parameters was not performed in the studies reported in Sec. 1.

At the BEP, the average velocity vectors are aligned with the blades, while velocity fluctuations over time remain minimal. This condition is achieved through a certain balance of forces (inertial, viscous, apparent forces) in the impeller. The effects of this balance are translated in the form of favorable performance coefficients, such as the pump efficiency itself, which reaches a maximum value. On the other hand, in operations away from the BEP, the forces acting on the impeller change the flow structure, the frequent presence of velocity fluctuations promoting the increase of energy losses in the pump stage. This situation, associated with a certain combination of quantities such as N, $\dot{m}$, and ΔP, leads the pump efficiency indicators to decrease.

Subsection 3.2 extends the results by describing the influence of the angular position (θ) on the

15

relative velocity vectors ($\vec{u}$) that compose the ensemble-average velocity fields. Then, the analysis of velocity fields is expanded in Subsection 3.3, which presents and discusses the velocity profiles measured at various radial and circumferential positions of the impeller channels.

3.2. Influence of the angular position on the relative velocity fields

As stated in Subsection 2.4, the experiments were conducted at three different angular positions measured by the encoder in the pump shaft, i.e., $\theta = [0°, 10°, 30°]$. Subsection 3.1 addressed results for $\theta = 0°$, while the current subsection aims to investigate results at $\theta = 10°$ and $\theta = 30°$. This comparison is made in Fig. 10 for $N = 900$ rpm and three water flow rates that correspond to shut-off, BEP, and open-flow conditions.

For both angular positions, the flow morphology under the shut-off condition (Figs. 10a and 10b) is characterized by the presence of vortices, in partially blocked channels, mainly to the left of the image. In this region, the impeller outlet is close to the volute spiral, which increases the interaction between the fluid and the solid walls. Regarding the BEP (Figs. 10c and 10d), the velocity field is well-behaved, and the streamlines tend to follow the curvature of the blades, as observed by Li et al. [28] as well. Finally, at the open-flow condition (Figs. 10e and 10f), there is a reduction in the water velocity on the pressure surface of the blades, with the streamlines deviating toward the suction and pressure blades, respectively. The same results are valid for $N = 600$ rpm.

It is evident that the angular position in which the images are captured does not significantly affect the ensemble-averaged flow fields. Therefore, as θ does not cause relevant changes in the velocity vectors, the next subsections will focus on a single angular position of the impeller, $\theta = 0°$.

3.3. Velocity profiles and the influence of flow rate, planar position, and proximity to volute tongue

Each vector of ensemble-averaged relative velocity ($\vec{u}$) from the last subsections can be written as a sum of a radial component with a tangential component, $\vec{u} = \vec{u_r} + \vec{u_t} = u_r \hat{e}_r + u_t \hat{e}_t$, where $\hat{e}_r$ and $\hat{e}_t$ are the unit vectors that define the r and t directions. Thus, in a polar coordinate system, a positive radial velocity comprises the fluid flowing from the inner to the outer radius of the impeller. A positive tangential velocity represents the fluid flowing in the counterclockwise direction, from the suction side of a blade to the pressure side of another blade, in each channel.

From this definition, the current subsection aims to compare relative velocity profiles of u_r and u_t in different conditions. The velocity profiles are investigated in three radial positions $r = [27, 38, 50]$ mm as displayed in Fig. 11. These positions, when normalized by the outer
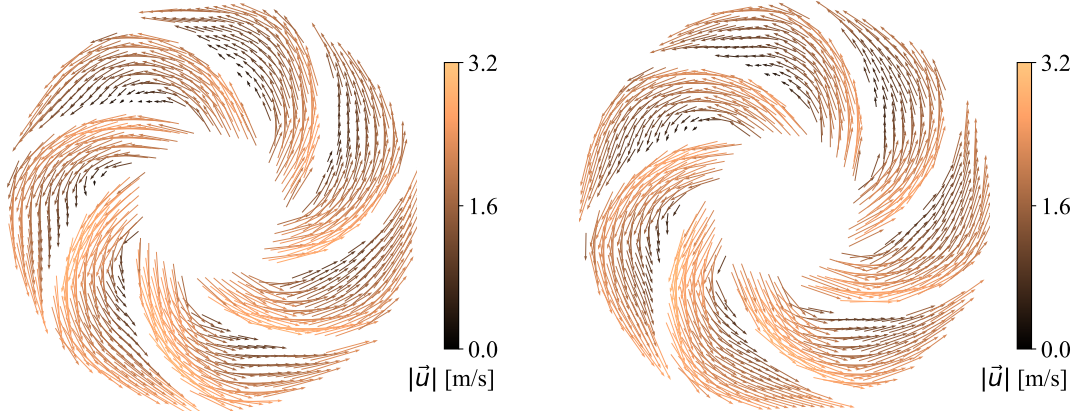
16
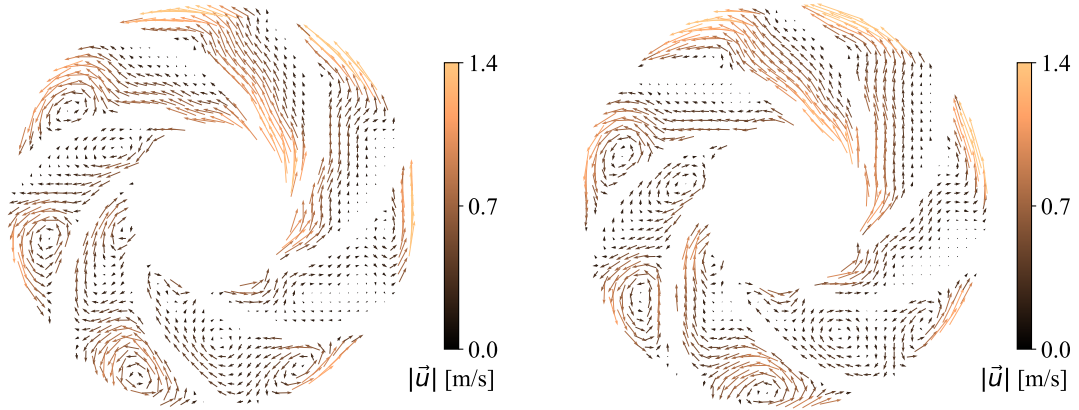
(a) $\dot{m} = 0.1 \ \dot{m}_{BEP}$ and $\theta = 10°$

(b) $\dot{m} = 0.1 \ \dot{m}_{BEP}$ and $\theta = 30°$
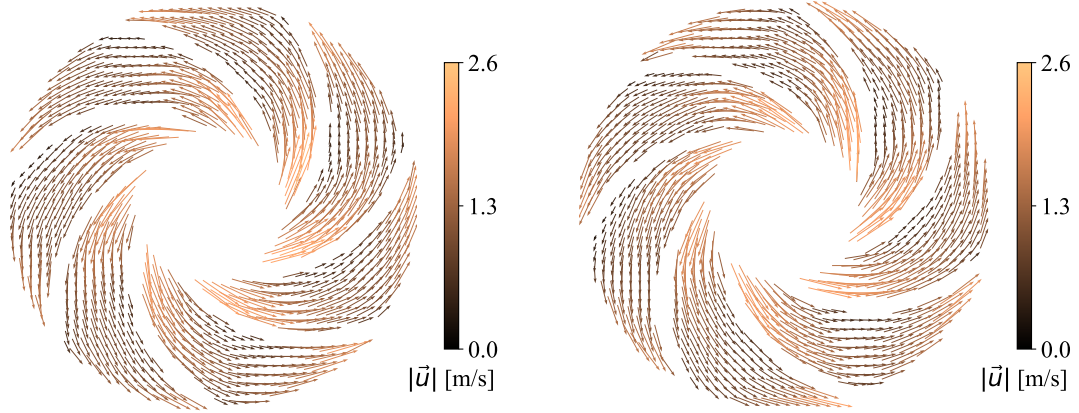
(c) $\dot{m} = 1.0 \ \dot{m}_{BEP}$ and $\theta = 10°$

(d) $\dot{m} = 1.0 \ \dot{m}_{BEP}$ and $\theta = 30°$

(e) $\dot{m} = 1.6 \ \dot{m}_{BEP}$ and $\theta = 10°$

(f) $\dot{m} = 1.6 \ \dot{m}_{BEP}$ and $\theta = 30°$

Figure 10: Relative velocity fields for $N = 900$ rpm at two different angular positions.

17

radius of the impeller, correspond to $r^* = r/r_o = [0.5, 0.7, 0.9]$. The analysis is performed in two channels, CA and CB, indicated in Fig. 11. As observed, CA is the channel furthest from the volute tongue, while CB is the channel closest to the volute tongue. Each channel is placed in different circumferential positions defined by the angle c as illustrated in Fig. 11 as well.

(a) $\dot{m} = 0.1\, \dot{m}_{BEP}$ (b) $\dot{m} = 1.0\, \dot{m}_{BEP}$ (c) $\dot{m} = 1.6\, \dot{m}_{BEP}$
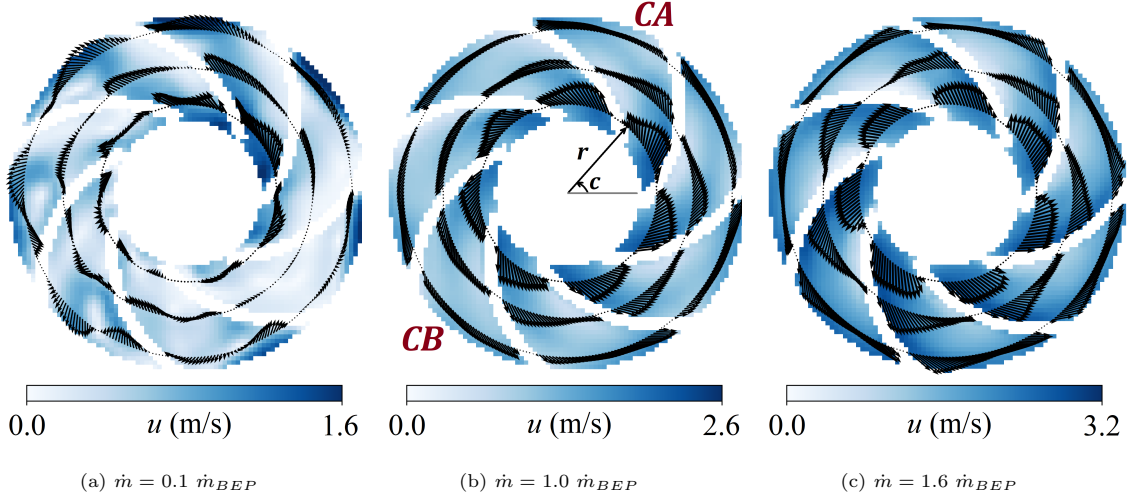
Figure 11: Velocity vectors (black) plotted superimposed on velocity magnitudes (blue) in three radial positions $r/r_o = [0.5, 0.7, 0.9]$ for three flow rates at $N = 900$ rpm.

The velocity profiles are depicted in Figs. 12 and 13 for channel CA and channel CB, respectively, for $N = 900$ rpm. In the x-axis, the normalized circumferential position c^* is calculated so that $c^* = 0.0$ corresponds to the surface of the suction blade (SB) and $c^* = 1.0$ refers to the surface of the pressure blade (PB) in each channel. Thus, $c^* = (c - c_{SB})/(c_{PB} - c_{SB})$. Furthermore, in the y-axis, the velocities u_r and u_t are normalized by the magnitude of the tangential velocity due to the impeller rotation, Ωr, calculated in the blade tip at the channel exit, where $r = r_o$:

$$|\vec{u}_r^*| = \frac{|\vec{u}_r|}{\Omega r_o} \quad \text{and} \quad |\vec{u}_t^*| = \frac{|\vec{u}_t|}{\Omega r_o} \tag{2}$$

The curves presented in each graph of Figs. 12 and 13 highlight the influence of $\dot{m}$ on u_r. As a general rule, a higher flow rate is associated with a higher radial velocity, and vice-versa. As the channel has a geometry comparable to a divergent nozzle, the radial velocity tends to decrease as the radial position increases. This trend is observed by comparing Figs. 12a, 12c and 12e, for example. The shape of the velocity profiles also depend on the flow rate. In the middle of the

18

channel, for instance, Fig. 12c reveals that the u_r is higher near the pressure blade (PB) when $\dot{m} \leq 0.3 \, \dot{m}_{BEP}$, while u_r is higher near the suction blade (SB) when $\dot{m} \geq 0.8 \, \dot{m}_{BEP}$.

The comparison between Figs. 12 and 13 indicates significant differences between channels CA and CB, especially at low flow rates. In the channel closest to the volute tongue, the radial velocity curves related to 0.1 $\dot{m}_{BEP}$ and 0.3 $\dot{m}_{BEP}$ have negative values, as depicted in Figs. 13a, 13c and 13e. The negative u_r values coincide with regions of the impeller where there are vortices and reverse flow. These structures were detected in the fields shown in Fig. 9. Thus, the velocity profiles corroborate and complement the velocity fields presented in Subsection 3.1.

Negative values are also identified in the tangential velocity curves, as observed in Figs. 13b, 13d and 13f. A negative u_t means that the relative velocity vector $\vec{u}$ has a tangential component aligned with the clockwise direction - something unexpected in an impeller composed of backward-curved vanes. This is an evidence of a very disordered flow topology, which occurs at low flow rates, as confirmed in Fig. 9. To complement this analysis, Subsection 3.4 brings an evaluation of absolute velocity fields that consider the tangential velocity due to the impeller motion.

For high flow rates, the u_t values are positive, as the flow tries to follow the blade curvature. However, the angle of the flow (defined by comparing u_r and u_t) is still different from the angle of the blade curvature (a geometric characteristic of the impeller). An analysis of this misalignment between velocity vectors and blade curvature is the main topic of Subsection 3.5.

3.4. Absolute velocity fields in the impeller and volute

From the average relative velocity ($\vec{u}$) determined through the PIV tests, it is possible to calculate the absolute velocity ($\vec{U}$) by adding the tangential component due to the impeller motion, which depends on the radial position ($\vec{r}$) and angular speed ($\vec{\Omega}$) vectors in the impeller: $\vec{U} = \vec{u} + \vec{\Omega} \times \vec{r}$. In polar coordinates, the cross product $\vec{\Omega} \times \vec{r}$ provides a vector, aligned with the direction $\hat{e}_t$, which must be added to $\vec{u}_t$. This vector is the only difference between the relative velocity (previous subsection) and the absolute velocity (current subsection).

Examples of ensemble-average absolute velocity fields are available for $N = 900$ rpm in Fig. 14, where vectors $\vec{U}$ (grey) are plotted over magnitude $|\vec{U}|$ contour plots (colors). The absolute velocity is clearly higher than the relative velocity, due to the effect of the impeller velocity, which acts in the clockwise direction. The intensity of the tangential term reaches $\Omega r = -5.0$ m/s in the blade tip at the channel exit, where $\Omega = -94.2$ rad/s and $r = r_o = 0.055$ m. Measurements were performed along a channel and a portion of the volute, on the right side of the pump, as indicated

19

(a) Radial velocity term (u_r) at $r/r_o = 0.5$

(b) Tangential velocity term (u_t) at $r/r_o = 0.5$

(c) Radial velocity term (u_r) at $r/r_o = 0.7$

(d) Tangential velocity term (u_t) at $r/r_o = 0.7$

(e) Radial velocity term (u_r) at $r/r_o = 0.9$
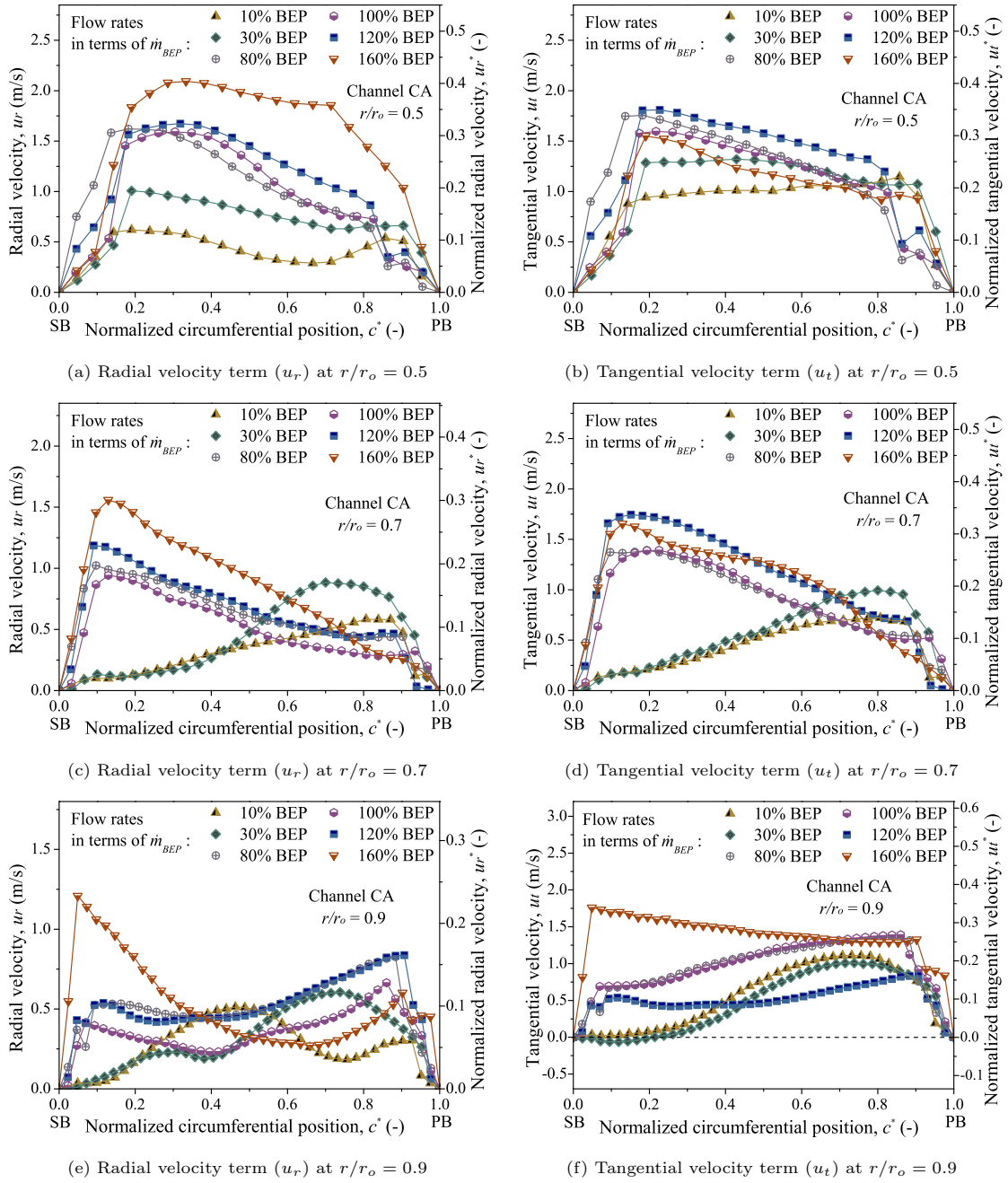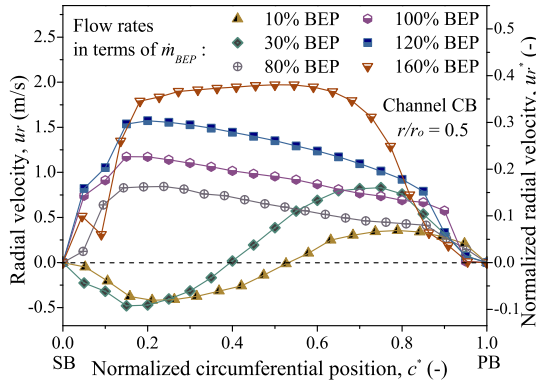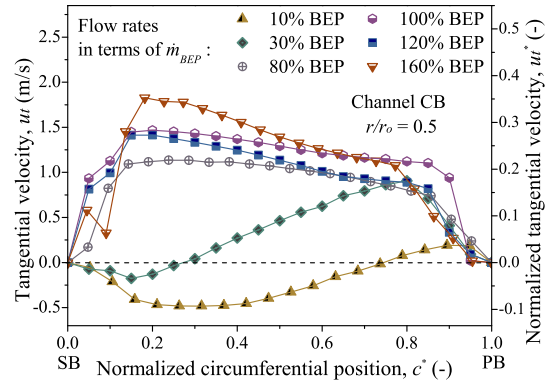
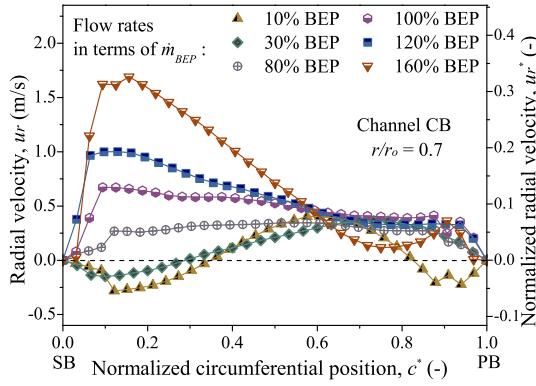(f) Tangential velocity term (u_t) at $r/r_o = 0.9$

Figure 12: Polar components of the relative velocity for $N = 900$ rpm in Channel CA.
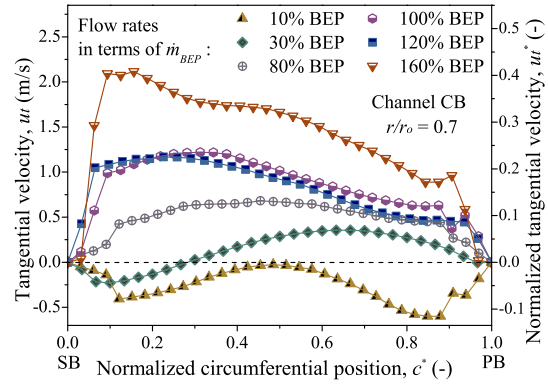
20

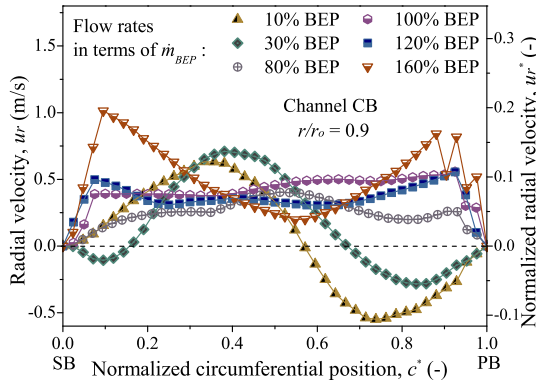(a) Radial velocity term (u_r) at $r/r_o = 0.5$

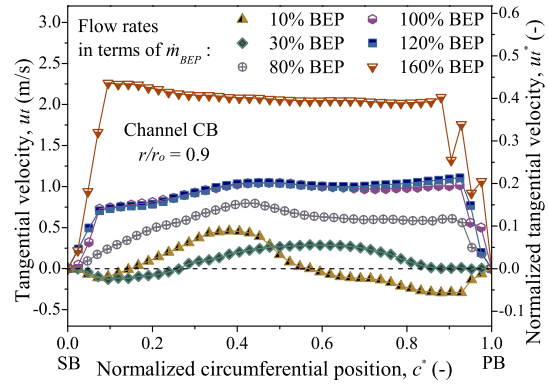(b) Tangential velocity term (u_t) at $r/r_o = 0.5$

(c) Radial velocity term (u_r) at $r/r_o = 0.7$

(d) Tangential velocity term (u_t) at $r/r_o = 0.7$

(e) Radial velocity term (u_r) at $r/r_o = 0.9$

(f) Tangential velocity term (u_t) at $r/r_o = 0.9$

Figure 13: Polar components of the relative velocity for $N = 900$ rpm in Channel CB.

by the black curve drawn in Fig. 14-BEP. The results are depicted in Fig. 15, which shows the velocity magnitude, $|\vec{U}|$, as a function of the radial position normalized by the outer radius, r/r_o.
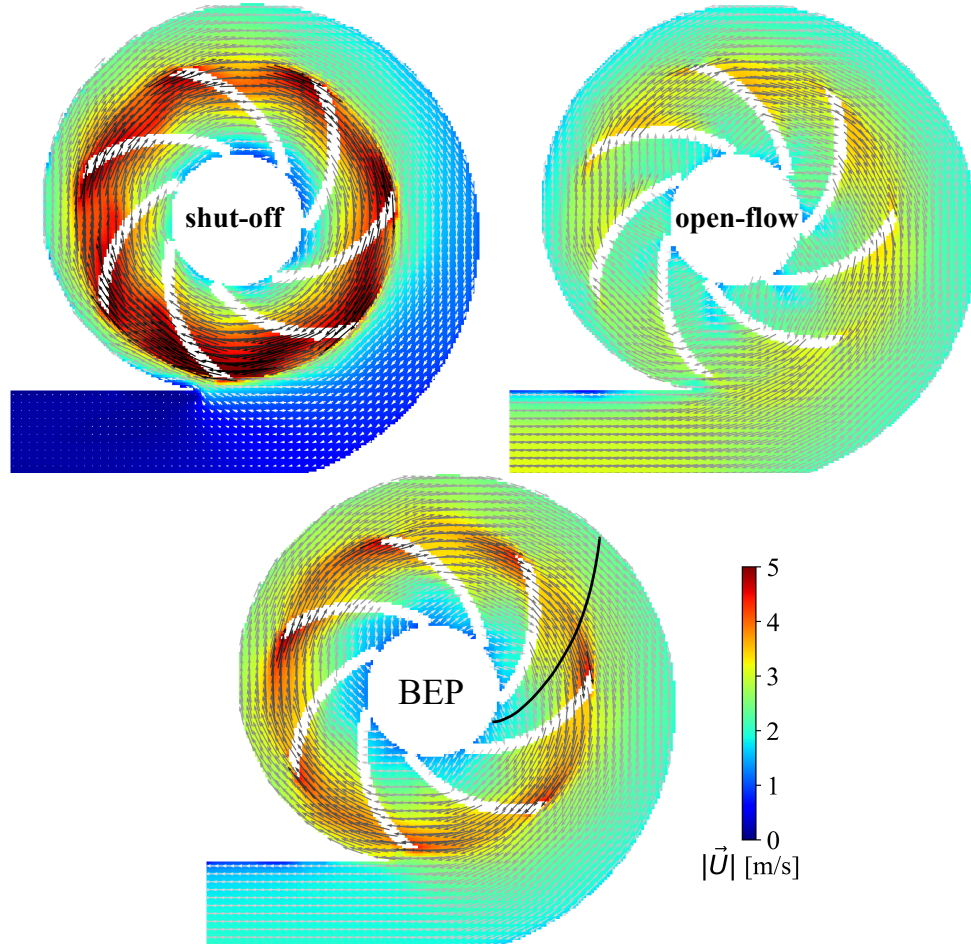
Figure 14: Absolute velocity vectors for $N = 900$ rpm and $\theta = 0°$. Stationary frame of reference.

At the minimum flow rate (shut-off, red curve in Fig. 15), the maximum value of the absolute velocity occurs at the impeller outlet, $r/r_o \approx 1.0$, as a result of the vector sum of a pronounced Ωr component with a reduced relative velocity. The exit region of the impeller is also associated with a sudden change in the velocity field, due to the boundary region between the rotating impeller and the stationary volute. Nevertheless, the absolute velocity intensity progressively decreases in the impeller as the water flow rate increases (BEP, green curve in Fig. 15), until reaching the maximum flow rate (open-flow, blue curve in Fig. 15).

22

Figure 15: Absolute velocity magnitude as a function of the radial position, for $N = 900$ rpm and three flow rates.
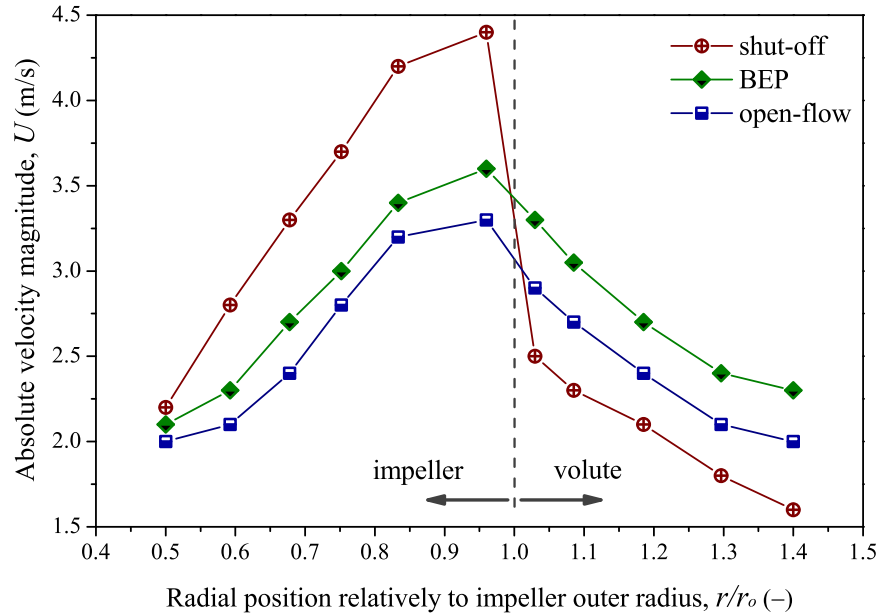
In the latter case, the relative velocity vectors have a high magnitude in radial outward (u_r) and tangential counterclockwise (u_t) directions, as discussed before in Figs. 12 and 13 in the last subsection. The counterclockwise direction of $\vec{u}$ is opposed to the clockwise direction of the $\vec{\Omega} \times \vec{r}$ term, so that the sum of the vectors results in an $\vec{U}$ better distributed along the impeller, without relevant discontinuities. The same behavior is identified at $N = 600$ rpm, in which the maximum tangential term is $\Omega r = -3.5$ m/s. Despite this difference in the velocity magnitudes, the flow topology is virtually the same for both rotational speeds. Therefore, the contour plots for $N = 600$ rpm have been suppressed as they do not add new information to the discussions developed here.

Going back to the relative velocity, Subsection 3.5 below investigates how the direction of the velocity vectors changes as a function of the flow rate and deviates from the blade curvature.

3.5. Deviation between velocity vectors evaluated through a cross product

As stated in Subsection 3.3, the average velocity vectors computed from the PIV experiments can be written in polar coordinates. However, these vectors are originally determined in a cartesian system, since the interrogation windows from the PIV processing methodology compose a grid on the xy plane. Without any components in z, it is possible to write $\vec{u} = \vec{u}_x + \vec{u}_y = u_x \hat{e}_x + u_y \hat{e}_y$,

23

where $\hat{e}_x$ and $\hat{e}_y$ are the unit vectors in the x and y directions. Therefore, for a position (x, y) in the impeller, the comparison of a vector $\vec{u}$ with its correspondent $\vec{u}_{BEP}$ obtained at the BEP may be an interesting strategy to investigate the characteristics of the water flow. In this sense, the cross product between $\vec{u}$ and $\vec{u}_{BEP}$ offers an estimation of the alignment between these vectors, measured by the sine of the angle ϕ, calculated as:

$$\phi = \arcsin\left(\frac{\vec{u}}{|\vec{u}|} \times \frac{\vec{u}_{BEP}}{|\vec{u}_{BEP}|} \right) \tag{3}$$

so that a different ϕ is obtained for each interrogation window related to a single $\vec{u}$ and a single $\vec{u}_{BEP}$. Contour plots with ϕ as a function of $\dot{m}$ are depicted in Fig. 16 for $N = 900$ rpm.

The analysis of the angle ϕ reveals the direction of the deviation between vectors. In Fig. 16, the blue tones indicate the positions (x, y) where there are vectors $\vec{u}$ rotated clockwise relatively to the vectors $\vec{u}_{BEP}$, while the red tones provide the regions where $\vec{u}$ is misaligned with $\vec{u}_{BEP}$ in the counterclockwise direction. The vectors found at the BEP are used as a reference in the calculations because they are associated with the pump operation with minimum energy losses.

For the lowest flow rates (Figs. 16a and 16b), the scale encompasses the interval $\phi = [-90°, 90°]$. Therefore, the extreme values disclose the vectors perpendicular to each other, a situation valid in regions where vortices are detected. Then, under the $\dot{m} = 0.8 \, \dot{m}_{BEP}$ condition (Fig. 16c), the scale is limited to $\phi = [-30°, 30°]$. In the channels of the first and second quadrants, the deviation occurs in clockwise direction, while in the channels of the third and fourth quadrants, the deviation between $\vec{u}$ and $\vec{u}_{BEP}$ is counterclockwise. This is an interesting behavior that is basically the effect of the asymmetric geometry of the pump stage due to the presence of the volute spiral.

In two channels of the second quadrant, it is possible to identify regions in the suction blades where the deviation is greater than $30°$. At first glance, one may suspect that the large blue spots on the contour plot of Fig. 16c are a consequence of errors in the experiment execution or image processing. However, these blue regions are actually related to the flow dynamics. After conducting another test and processing a new sample of images, it was clear that there are stagnation zones in the vicinity of the suction blades of these channels at $\dot{m} = 0.8 \, \dot{m}_{BEP}$.

The BEP is used as a reference in Fig. 16d, where $\phi = 0°$ in the entire impeller. Subsequently, for $\dot{m} = 1.2 \, \dot{m}_{BEP}$ (Fig. 16e), the deviations reach $30°$ again. The comments made for Fig. 16c are also valid for Fig. 16e, except for the statements about the stagnation zones, which are no longer observed. The last contour plot finally addresses the misalignment at the highest flow rate

24

(a) $\dot{m} = 0.1\ \dot{m}_{BEP}$

(b) $\dot{m} = 0.3\ \dot{m}_{BEP}$

(c) $\dot{m} = 0.8\ \dot{m}_{BEP}$

(d) $\dot{m} = 1.0\ \dot{m}_{BEP}$ (reference)

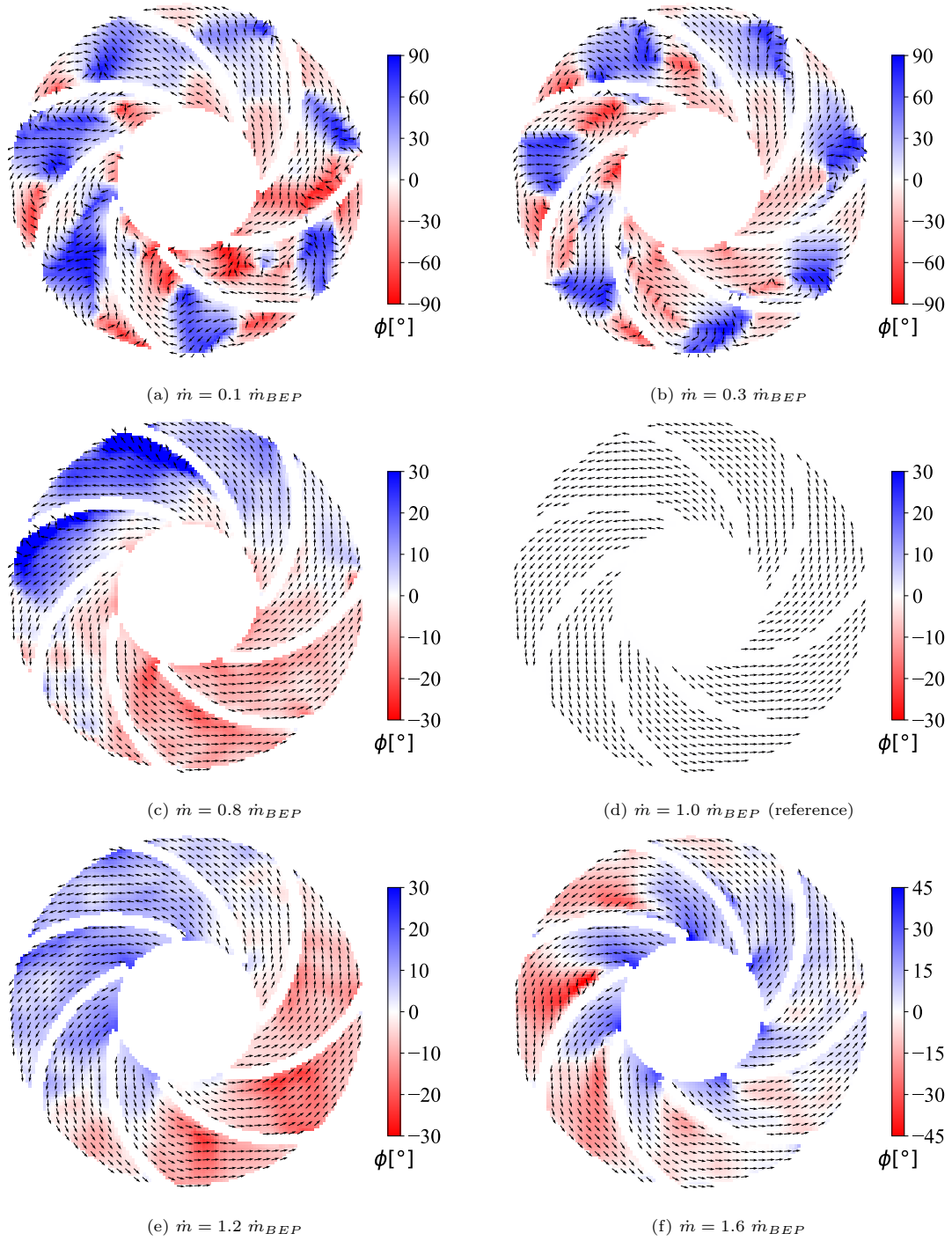(e) $\dot{m} = 1.2\ \dot{m}_{BEP}$

(f) $\dot{m} = 1.6\ \dot{m}_{BEP}$

Figure 16: Misalignment ϕ between velocities at $N = 900$ rpm measured by the cross product.

25

(Fig. 16f). In this case, the channels generally mix regions with clockwise (blue) and counterclock-
wise (red) deviations, with angles in the range $\phi = [-45°, 45°]$. This trend indicates a change in
the direction of the velocity vectors, which deflect toward the suction blades in the first half of the
fluid path, and then deflect toward the pressure blades in the second half.

Such results corroborate the observations made in Subsection 3.1, in particular in Fig. 9. Be-
sides, as there is a remarkable similarity between the flow fields at different rotational speeds, the
analyses made above for $N = 900$ rpm are also valid for $N = 600$ rpm. Two similar $\dot{m}$ relative to
fractions or multiples of $\dot{m}_{BEP}$ tend to produce similar velocity fields regardless of N.

The results presented in Fig. 16 help understand the shock losses in the impeller inlet region.
For lower flow rates, the flow is more affected by apparent forces, so that $\phi < 0°$ (red) at $r \approx r_i$.
For higher flow rates, the flow moves faster and tends to have a radial direction, so that $\phi > 0°$
(blue) in the same entrance region. This variation on the vector angles was also observed by Li et
al. [39] and interpreted as a source of energy losses when the pump operates away from the BEP.

Another interesting observation in Fig. 16 is related to flow recirculation. The distribution
of ϕ in the impeller reveals that the flow direction changes twice at the shut-off (Fig. 16a), in
a red-blue-red pattern found in each channel. At the open-flow (Fig. 16f), on the contrary, the
direction changes once, in a blue-red pattern. Thus, the number of transition zones depends on
the flow rate and may quantify the intensity of flow recirculation in the channels.

These results can be further explored through an analysis of vorticity and turbulence in the
pump. Subsection 3.6 evaluates the vorticity while Subsection 3.7 addresses the turbulence in the
pump stage, for $\phi = 0°$, $N = 900$ rpm, and six different water flow rates as listed in Tab. 1.

3.6. Vorticity in the impeller and volute

From the perspective of continuum mechanics, vorticity is a way of describing the tendency
of the fluid particles to rotate at a given point. Vorticity is essentially a vector defined by the
curl of the relative or absolute velocities. In the current paper, as these velocities are computed
on the xy plane, the vorticity vector has only the term in the z direction. The images acquired
during the PIV tests are divided into interrogation windows, so that each window has a velocity
vector valid for a single position. Therefore, as the water velocity is discrete, its derivatives must
be calculated via numerical methods. In this paper, vorticity (ω_z) is computed using the centered
finite difference method [40].

The vorticity calculated from relative velocities is defined as $|\vec{\omega}_{z_{rel}}| = \partial u_y / \partial x - \partial u_x / \partial y$, while

26

that from absolute velocities is $|\vec{\omega}_{z_{abs}}| = \partial U_y / \partial x - \partial U_x / \partial y$. Then, following the method used by Keller [38], a normalized vorticity ω_z^* is defined by dividing the vorticity ω_z by the solid rotation of the impeller, whose intensity is 2Ω:

$$|\vec{\omega}_{z_{rel}}^*| = \frac{|\vec{\omega}_{z_{rel}}|}{2\Omega} \quad \text{and} \quad |\vec{\omega}_{z_{abs}}^*| = \frac{|\vec{\omega}_{z_{abs}}|}{2\Omega} \tag{4}$$

Figure 17 presents six contour plots with the normalized vorticity calculated from the relative velocity in the impeller, for $N = 900$ rpm, and flow rates from the shut-off to open-flow conditions, according to Tab. 1. At low flow rates (Figs. 17a and 17b), the locations with maximum vorticity coincide with the positions of the vortices. A negative vorticity is associated with vortices that rotate clockwise, which frequently occur at the entrance of the channels. Conversely, a positive vorticity is related to the vortices that rotate counterclockwise, which are closer to the impeller exit. According to Keller [38], these vortices are the effect of the adverse pressure gradient, with consequent flow separation at the blade tip, in addition to the tendency of the flow to maintain its angular momentum and, thus, to perform a rotation in a direction opposite to that of the impeller.

Under the conditions between 80% and 120% of the BEP (Figs. 17c, 17d, 17e), the distribution of $\omega_{z\,rel}^*$ along the impeller is approximately equal in all channels, with regions of positive vorticity in the center and negative vorticity on the surfaces of the blades. The magnitude of the vorticity is relatively low at these flow rates closer to the $\dot{m}_{BEP}$, in which the flow is more uniform and the streamlines are aligned with the blades.

At high flow rates (Fig. 17f), the entire area of the impeller contains a positive vorticity, indicating a trend of rotation of the fluid in a counterclockwise direction. This is the result of the flow concentration on the suction blades [38]. As mentioned above, the streamlines undergo a deviation while the velocity near the pressure blades decreases. Thus, at flow rates above the design condition, we observe that the flow in each channel has a structure comparable to half a large vortex rotating counterclockwise.

The same discussion is valid for $N = 600$ rpm, whose contour plots show similar distributions and magnitudes of $\omega_{z\,rel}^*$ as a function of (x, y) and $\dot{m}$. The results presented here complement the observations made in Subsections 3.1 and 3.3, in particular the flow fields depicted in Fig. 9 and profiles shown in Figs. 12 and 13.

The estimation of the vorticity was extended for the complete stage, considering the absolute velocity, with its tangential component proportional to the impeller radius and rotational speed.

27

(a) $\dot{m} = 0.1 \; \dot{m}_{BEP}$

(b) $\dot{m} = 0.3 \; \dot{m}_{BEP}$

(c) $\dot{m} = 0.8 \; \dot{m}_{BEP}$

(d) $\dot{m} = 1.0 \; \dot{m}_{BEP}$

(e) $\dot{m} = 1.2 \; \dot{m}_{BEP}$
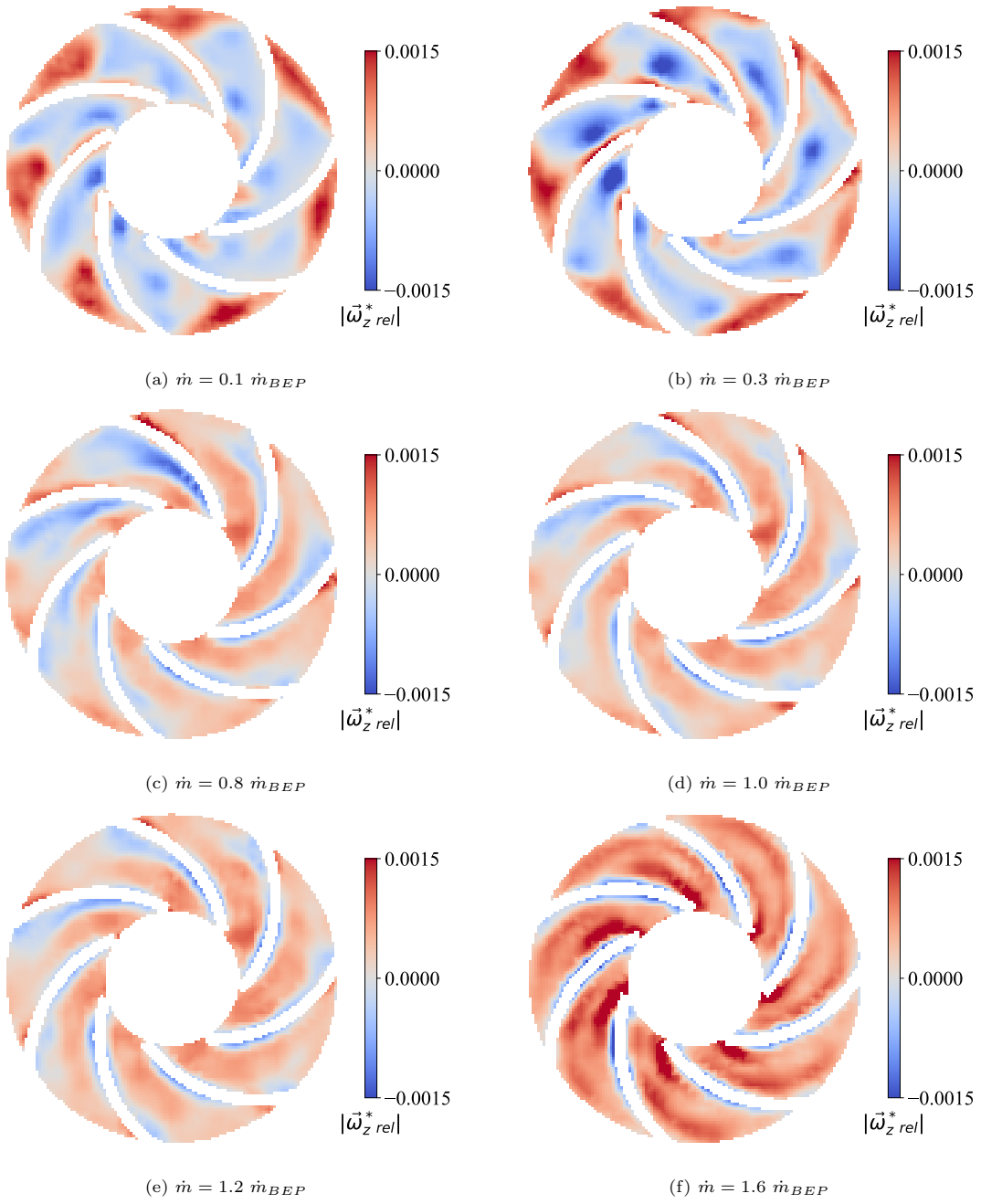
(f) $\dot{m} = 1.6 \; \dot{m}_{BEP}$

Figure 17: Normalized vorticity in the impeller, obtained from relative velocities, for $N = 900$ rpm.

Figure 18 shows new contour plots with the normalized vorticity calculated from the absolute velocity in the entire pump stage, for $N = 900$ rpm, and flow rates from shut-off to open-flow.

In all conditions analyzed, it is possible to verify that the predominant vorticity in the impeller changed from positive (red tones) to negative (blue tones) when the velocity evaluated in the calculations changed from relative ($\vec{u}$) to absolute ($\vec{U}$). This fact occurs due to the addition of the impeller velocity, which acts in the clockwise direction with a magnitude proportional to Ωr.

At lower flow rates (Figs. 18a and 18b), the border region between the impeller and the volute showed the highest positive values of $\omega^*_{z\,abs}$. This is the effect of the difference between the water velocities in the impeller (rotating, with the term Ωr) and in the volute (stationary, without the term Ωr), as shown before in Figs. 14 and 15. Such results are also relevant for two-phase flows: when the pump operates in presence of liquid-liquid dispersions, for example, these significant changes in the vorticity of the continuous phase influence the behavior and dynamics of the dispersed phase as well. The conditions found in the impeller-volute boundary intensify the deformation and fragmentation of dispersed drops, thus promoting the formation of oil/water or water/oil emulsions, a common issue in pump applications related to the oil and gas industry [41].

However, as the flow rates increase (Figs. 18c, 18d, 18e) and reach higher values (Fig. 18f), the vorticity in the center of the channels becomes quite low. The influence of the component Ωr on the absolute velocity (clockwise) is counterbalanced by the intense relative velocity (counterclockwise) normally associated with high flow rates, as addressed in Subsection 3.3 - Figs. 12 and 13. Regions with significant $\omega^*_{z\,abs}$ include the surfaces of the blades, the beginning of the spiral, and the exit of the volute. The pump studied by Keller [38] had a similar behavior, interpreted by the author as a consequence of the detachment of the boundary layer in the vicinity of the solid walls.

Again, the discussions are also valid for $N = 600$ rpm, with contour plots presenting similar distributions and magnitudes of $\omega^*_{z\,abs}$ as functions of (x, y) and $\dot{m}$. The results available in the current subsection complement the Subsection 3.4 and flow fields displayed in Fig. 14.

3.7. Turbulence in the impeller and volute

The turbulent kinetic energy (TKE) is the average energy per unit of mass associated with velocity fluctuations. The TKE value, symbolized by k, is calculated from variances of the velocity fluctuations in time, represented by $\overline{u'_x}$ and $\overline{u'_y}$ in the x and y directions, respectively [38]:

$$k = \frac{\left(\overline{u'_x}\right)^2 + \left(\overline{u'_y}\right)^2}{2} \tag{5}$$

29

(a) $\dot{m} = 0.1\ \dot{m}_{BEP}$

(b) $\dot{m} = 0.3\ \dot{m}_{BEP}$

(c) $\dot{m} = 0.8\ \dot{m}_{BEP}$

(d) $\dot{m} = 1.0\ \dot{m}_{BEP}$

(e) $\dot{m} = 1.2\ \dot{m}_{BEP}$
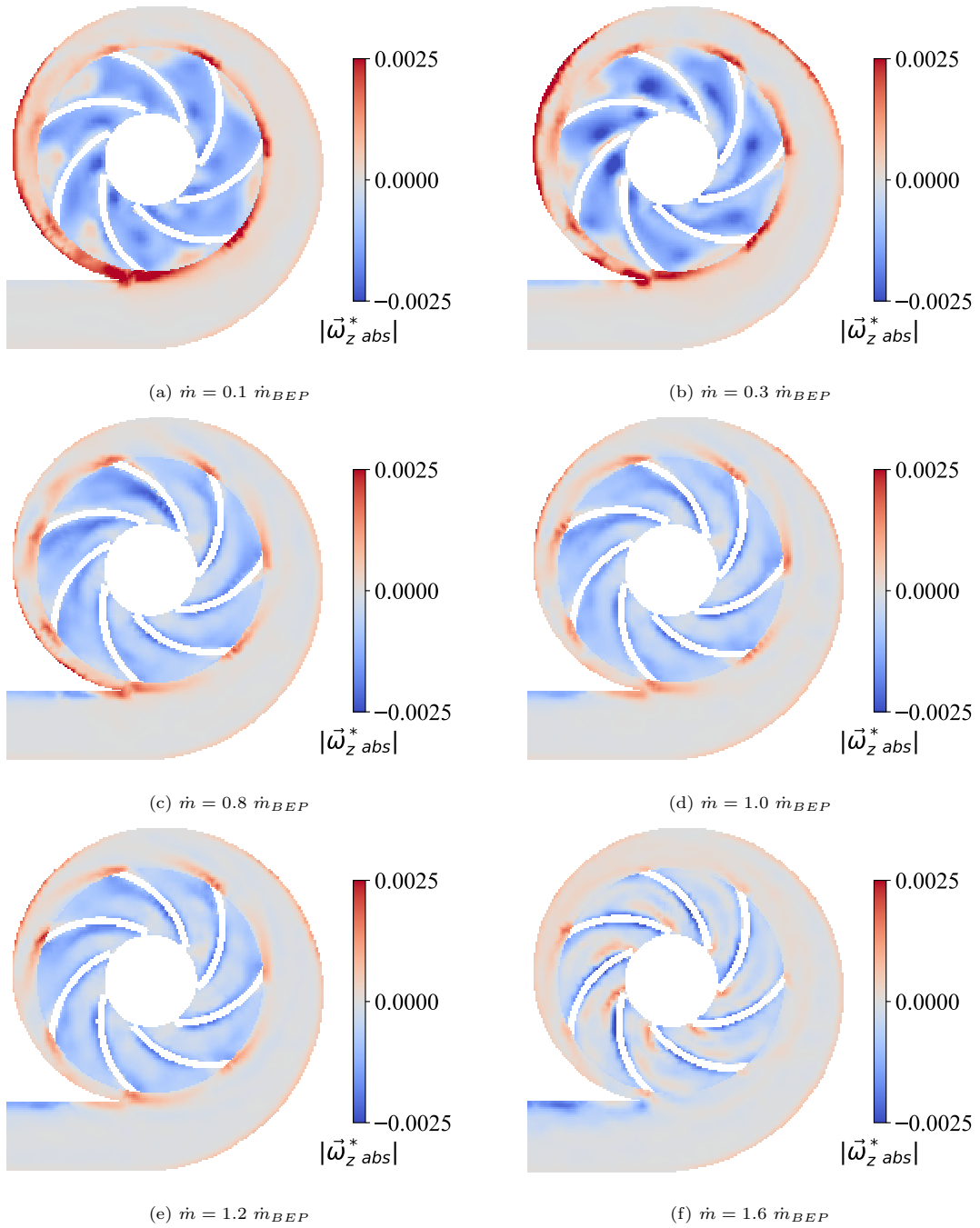
(f) $\dot{m} = 1.6\ \dot{m}_{BEP}$

Figure 18: Normalized vorticity in the pump stage, obtained from absolute velocities, for $N = 900$ rpm.

In theory, the variances should be evaluated in the interval between initial (t_i) and final (t_f) time instants. For example, in the x direction, $\overline{(u_x')}^2 = \frac{1}{t_f - t_i} \int_{t_i}^{t_f} (u_{x(inst)}(t) - u_{x(avg)})^2 \, dt$, where $u_{x(inst)}$ is the instantaneous velocity and $u_{x(avg)}$ is the average velocity, both computed by the PIV method.

Numerically, however, the calculation of these velocity fluctuations is performed in each pair of PIV images, separated from the next pair by an interval Δt. As explained in Section 2, each average velocity is obtained from a sample of n images full of instantaneous velocities, i.e., $u_{x(avg)} = \frac{1}{n} \sum_{i=1}^{n} u_{x,i(inst)}$. Thus, the velocity variance in the x direction is simply:

$$\overline{(u_x')}^2 = \frac{1}{n} \sum_{i=1}^{n} (u_{x,i(inst)} - u_{x(avg)})^2 \tag{6}$$

In other words, the comparison between average and instantaneous velocity vectors, both found via PIV, provide the velocity fluctuations and their variances associated with each interrogation window. These variances are the basis for obtaining the TKE (Eq. 5). The final step is defining k^*, which is the TKE normalized by the linear velocity of the blade tip [38]:

$$k^* = \frac{k}{(\Omega r_o)^2} \tag{7}$$

where Ω is the angular velocity of the impeller and r_o its outer radius. Figure 19 shows six contour plots with the normalized TKE in the entire pump stage, for $N = 900$ rpm, $\theta = 0°$, and flow rates from shut-off to open-flow conditions.

The observation of Figs. 19a and 19b suggests that the lowest flow rates are related to an intense turbulent energy, especially at the exit of the channels and at the beginning of the volute spiral, where k^* assumes values higher than 0.012. As the water flow rate is very low, the fluid remains circulating through the volute, instead of leaving the pump stage. Then, when passing at the beginning of the spiral, the flow is accelerated and disturbed by the volute tongue, which intensifies the formation of turbulent wakes. The volute tongue promotes the formation of emulsions when the pump operates with two-phase liquid-liquid dispersions [41]. In this case, the tongue imposes a shear stress in the flow, which causes the drops to gradually deform and break-up.

The analysis of Figs. 19c, 19d, 19e reveals that the pump has lower energy losses due to turbulence when operating around the design condition. The regions where the TKE is more relevant include the center of the channels and the impeller-volute boundary, where k^* reaches 0.004. Similar results were obtained by Keller [38], but the author claims that these turbulence
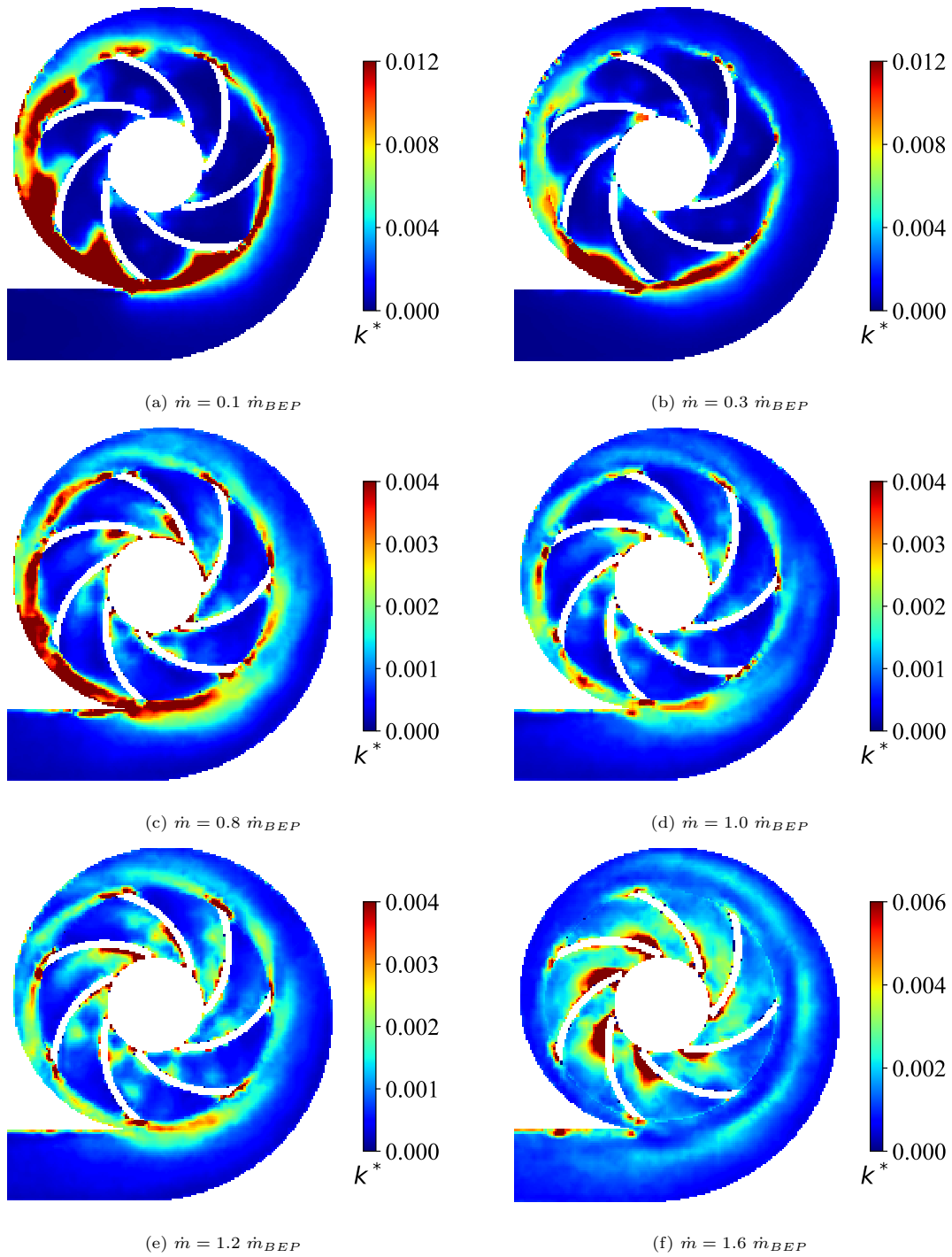
31

(a) $\dot{m} = 0.1\ \dot{m}_{BEP}$

(b) $\dot{m} = 0.3\ \dot{m}_{BEP}$

(c) $\dot{m} = 0.8\ \dot{m}_{BEP}$

(d) $\dot{m} = 1.0\ \dot{m}_{BEP}$

(e) $\dot{m} = 1.2\ \dot{m}_{BEP}$

(f) $\dot{m} = 1.6\ \dot{m}_{BEP}$

Figure 19: Normalized turbulent kinetic energy in the pump stage for $N = 900$ rpm.

levels are a consequence of: 1) The flow separation caused by the tips of the blades; 2) the detachment of the boundary layer along the solid surfaces of the blades; and also 3) the variations in the water velocity at the impeller exit region.

Finally, by observing Fig. 19f at the highest flow rate, it is possible to verify that the zones with higher TKE are close to the pressure surfaces of the blades, where $|\vec{u}|$ is low and k^* reaches 0.006. Pump turbulence is thus a result of the concentration of the flow next to the suction blades, a phenomenon reported in the previous pages. The flow acquires a shape comparable to that of a large vortex, associated with the detachment of the boundary layer from the pressure blade surface, where intense velocity fluctuations generate intense values of TKE.

When comparing Fig. 19f with other turbulence plots, it can be seen that k^* is very low at the blade tips and impeller-volute boundary. This result is probably related to the intense velocities found at the open flow. As the flow rate and relative velocity increase, the influence of the impeller rotation becomes relatively less important, the flow leaving the impeller without being severely affected by the impeller motion. As addressed above in Figs. 14 and 15, the open-flow condition is associated with the lowest absolute velocity differences in the impeller outlet.

The results presented in this subsection complement those ones available in the previous pages, especially in Subsections 3.1 and 3.6. The same discussions made for $N = 900$ rpm are also valid for $N = 600$ rpm, thus the results regarding this last rotational speed were not included, as they would not add new information to the analysis.

As reported in the last paragraphs, each interrogation window of an image pair has a single value of TKE, calculated from the velocity fluctuations. In this sense, the sum of each k, in each of these N_{IW} windows, may express an interesting way of evaluating the total energy loss due to turbulence in the impeller as a whole:

$$k_{sum} = \sum_{i=1}^{N_{IW}} k_i \tag{8}$$

The summed TKE (k_{sum}) can afterwards be divided by the summed TKE computed at the BEP ($k_{sum\,BEP}$), so that a normalized summed TKE (k'_{sum}) is obtained:

$$k'_{sum} = \frac{k_{sum}}{k_{sum\,BEP}} \tag{9}$$

The result is available in Fig. 20 together with polynomial fits. In this case, the analysis covered the whole test matrix with 12 flow conditions, as presented in Tab. 1. Furthermore, a dimensionless

33

head curve is also drawn on the graph to help the reader identify the BEP.

As observed, k'_{sum} assumes values as high as 3.5 to 4.0 when the centrifugal pump operates at shut-off and open-flow conditions. The behavior of TKE as a function of the dimensionless water flow rate is represented by second-degree polynomials with coefficients of determination greater than $R^2 = 0.88$. The minimum point of the parabolas occur at the BEP, in which k'_{sum} is unitary. This fact thus corroborates the idea that the maximum efficiency of the centrifugal pump is related to the occurrence of minimal energy losses due to turbulent effects. This is valid, at least, for single-phase low-viscous flows, such as the water flow studied here.

It is noticeable that there is a relevant similarity between the normalized summed TKE curves. The polynomial fit of $N = 600$ rpm is similar to the adjustment of $N = 900$ rpm. This fact stems from the similitude in the velocity fields (Subsection 3.1) observed when the pump operates at a given flow rate referenced in terms of BEP, regardless of the impeller rotational speed.
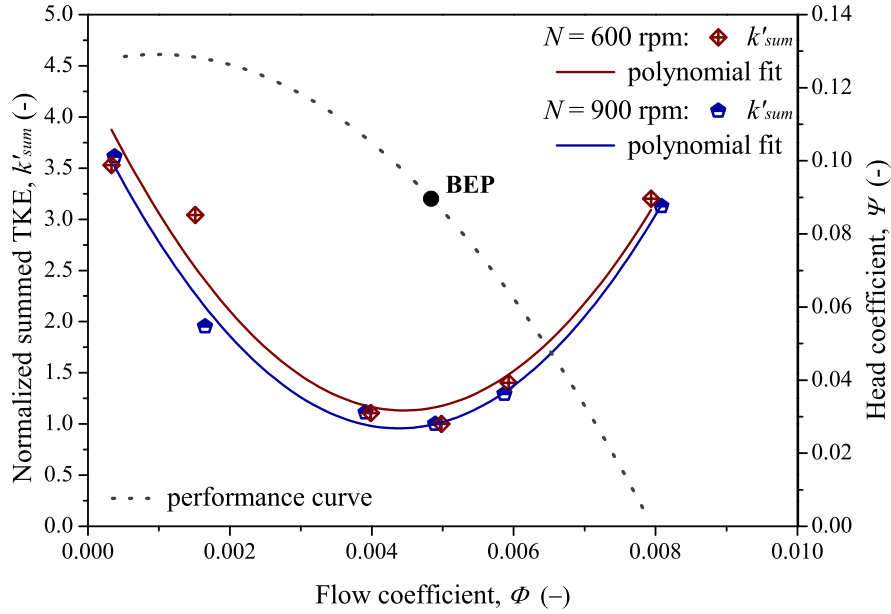

Figure 20: Total TKE in the impeller, referenced by the BEP, as a function of N and Φ, and adjusted by polynomials.

In view of everything discussed in Sec. 3, it is evident that the image acquisition and processing enabled the characterization of the single-phase water flow in the stage of the transparent centrifugal pump. In the scope of the PIV technique reported in Sec. 2, the results presented in this manuscript agree with - and complement - the observations made by other authors in the

same area of knowledge [25, 26, 27, 28, 29, 30, 31, 32, 33] whose studies were mentioned in Sec. 1.

An interesting contribution of this paper is the possibility of simultaneously analyzing all the impeller channels and also the entire volute spiral. The experimental program relied on a robust time-resolved visualization equipment, fluorescent tracer particles, and accurate instruments. A routine to process the PIV images was developed and adopted for obtaining absolute and relative ensemble-average velocity fields and contour plots with vorticity and turbulence levels. It was also possible to analyze the alignment of velocity vectors in comparison with the vectors found at the BEP, in which the energy losses should be minimal. Such losses were also evaluated by means of the total TKE, estimated throughout the impeller.

4. Conclusions

The main conclusions from the PIV results include the following:

1. The processed PIV images show that the operating conditions of the centrifugal pump strongly influence the flow behavior, or vice-versa. Therefore, quantities such as velocity, vorticity, and turbulence are dependent on the water flow rate. However, the angular position of the impeller, measured by the encoder, does not affect the results significantly.

2. Under low flow rates, near the shut-off condition, flow morphology is characterized by the presence of vortices in partially blocked channels. These vortices rotate in the clockwise and counterclockwise directions. They are associated with very intense vorticity and TKE that have maximum values at the interface between the impeller (rotating) and volute (stationary), where there is a relevant change in the absolute velocity, in addition to a separation of the flow caused by each blade tip.

3. At conditions close to the BEP, the velocity field is uniform and smooth, and the streamlines tend to follow the curvature of the impeller blades. The magnitude of the relative velocity is higher at the entrance and lower at the exit of each channel, whose geometry resembles a divergent nozzle. In addition, the velocity is higher in the channels to the right and lower in the channels to the left of the impeller, as a result of the interaction of the fluid with the solid walls that compose the volute spiral. Vorticity and turbulence are minimal when the pump operates at the BEP.

4. Under flow rates that correspond to 80% and 120% of the BEP, the relative velocity vectors deviate by up to 30° in relation to the vectors found exactly at the BEP. This misalignment depends on the position: it occurs clockwise in the first and second quadrants, but counterclockwise in the

35

third and fourth quadrants. Despite the deviations in these vectors, the vorticity and TKE remain at low values, comparable to those found when the pump operates with its maximum efficiency.

5. Under the conditions of a higher flow rate, close to the open-flow, there is a reduction in the average velocity on the pressure surface of the impeller blades. The streamlines undergo a deviation within the channels that generates a structure comparable to half a large vortex that rotates counterclockwise. The fluid path becomes longer and the boundary layer becomes detached. Such circumstances are related to very intense vorticity and turbulence in the vicinity of the pressure blades, where velocity fluctuations are significant.

6. The sum of TKE values in the entire domain of the impeller seems to be a function of the experimental condition. The minimum point of this quantity occurs at the BEP, while the highest values are found at the extreme flow rates corresponding to shut-off and open-flow. This is an indication that the energy losses due to turbulence are minimal when the pump efficiency is maximum, but they increase as the pump operation moves away from the design point.

7. Similar results are observed when the pump operates under conditions in which its performance is constant. In other words, the characteristics of two different flows are analogous as long as these flows are associated with the same dimensionless head and flow rate coefficients of the centrifugal pump. This is true even when the rotational speeds and the absolute flow rates are different. To exemplify this idea: The flow at $N_1 = 600$ rpm, $\dot{m}_1 = 1500$ kg/h has similar attributes as the flow at $N_2 = 900$ rpm, $\dot{m}_2 = 2200$ kg/h. Although N_1 and $\dot{m}_1$ are different from N_2 and $\dot{m}_2$, both conditions correspond to the pump's BEP. As the machine presents the same Ψ and Φ at these conditions, the flow within its stage is expected to be similar, regardless of the absolute values of N and $\dot{m}$.

Based on the conclusions reported above, we suggest the following future activities: 1) Perform new PIV tests with other fluids more viscous than water in order to evaluate the influence of viscosity on the characteristics of the single-phase flow in the pump stage; 2) extend the use of PIV methods for two-phase liquid-liquid flows to analyze the influence of a dispersed phase on the behavior of a continuous phase; 3) perform PIV tests in new impellers with other geometric attributes, extending the test matrix to higher rotational speeds, closer to those of commercial pumps.

36

List of Symbols

$\dot{m}$	-	Mass flow rate	[kg/h]
Q	-	Volumetric flow rate	[m^3/h]
Φ	-	Dimensionless flow rate	[-]
P	-	Pressure at the pump inlet	[kPa]
ΔP	-	Pressure increment provided by the pump	[kPa]
H	-	Pump head	[m]
Ψ	-	Dimensionless head	[-]
η	-	Pump efficiency	[-]
τ	-	Torque at the pump shaft	[N.m]
N	-	Impeller (and shaft) rotational speed	[rpm]
Ω	-	Impeller (and shaft) angular speed	[rad/s]
θ	-	Impeller (and shaft) angular position	[°]
r_i, r_o	-	Impeller inner and outer radius	[mm]
D	-	Impeller diameter	[mm]
h	-	Impeller blade height	[mm]
T	-	Water temperature	[°C]
ρ	-	Water density	[kg/m^3]
μ	-	Water viscosity	[Pa.s]
δt	-	Time interval between consecutive single pulses	[s]
Δt	-	Time interval between consecutive pairs of pulses	[s]
$\vec{u}$	-	Average relative velocity vector	[m/s]
$\vec{U}$	-	Average absolute velocity vector	[m/s]
$u_{(avg)}$	-	Average velocity value	[m/s]
$u_{(inst)}$	-	Instantaneous velocity value	[m/s]
$\overline{u'}$	-	Variance of velocity fluctuations in time	[m/s]
n	-	Number of images used to compute the average value	[-]
$\vec{r}$ or r	-	Radial position in the impeller	[m]
t or c	-	Tangential or circumferential position in the impeller	[rad]
u_r, u_t	-	Radial and tangential velocities (polar coordinates)	[m/s]
x, y	-	Horizontal and vertical positions in the impeller	[rad]

u_x, u_y	-	Horizontal and vertical velocities (cartesian coordinates)	[m/s]
ϕ	-	Deviation between $\vec{u}$ and $\vec{u}_{BEP}$	[°]
$\vec{\omega}_z$	-	Vorticity	[1/s]
ω_z^*	-	Normalized vorticity	[-]
k	-	Turbulent kinetic energy (TKE)	[m²/s²]
k^*	-	Normalized turbulent kinetic energy	[-]
k_{sum}	-	Total turbulent kinetic energy in the impeller	[m²/s²]
k'_{sum}	-	Normalized total turbulent kinetic energy in the impeller	[-]

Declarations

Ethical approval

Not applicable. This manuscript is not related to human and/or animal studies.

Competing interests

There are no interests of a financial or personal nature.

Authors' contributions

Conceptualization: Rodolfo Perissinotto and Rafael Cerqueira. Original draft preparation: Rodolfo Perissinotto, Rafael Cerqueira and William Fonseca. Review and editing: Rodolfo Perissinotto, Rafael Cerqueira, William Fonseca, Erick Franklin, Marcelo Castro, William Monte Verde, Jorge Biazussi and Antonio Bannwart. Supervision: Marcelo Castro. Project administration: Jorge

Biazussi and William Monte Verde. Funding acquisition: Antonio Carlos Bannwart and Marcelo
Castro. All authors have read and agreed to the published version of the manuscript.

Availability of data and materials

If requested by the journal or the reader, the authors can provide samples of the database used
to produce the results presented in this manuscript.

References

[1] D. Wilson, Turbomachinery: from paddle wheels to turbojets, Mechanical Engineering 104
(1982) 28–40.

[2] M. Volk, Pump characteristics and applications, CRC Press, 2013.

[3] R. Flatern, The defining series: electrical submersible pumps, Oilfield Review (2015) 1–2.

[4] G. Takacs, Electrical submersible pumps manual: design, operations, and maintenance, Gulf
professional publishing, 2017.

[5] A. Rosa, R. Carvalho, J. Xavier, Engenharia de reservatórios de petróleo, Editora Interciência,
2006.

[6] J. F. Gülich, Centrifugal pumps, Vol. 2, Springer, 2008.

[7] R. M. Perissinotto, W. Monte Verde, J. L. Biazussi, N. A. V. Bulgarelli, W. D. P. Fonseca,
M. S. d. Castro, E. d. M. Franklin, A. C. Bannwart, Flow visualization in centrifugal pumps:
A review of methods and experimental studies, Journal of Petroleum Science and Engineering
203 (2021) 108582.

[8] M. Raffel, C. E. Willert, J. Kompenhans, et al., Particle image velocimetry: a practical guide,
Vol. 2, Springer, 1998.

[9] A. J. Smits, Flow visualization: techniques and examples, World Scientific, 2012.

[10] J. Gamboa, M. Prado, et al., Visualization study of the performance breakdown in the two-phase performance of an electrical submersible pump, in: Proceedings of the 26th International Pump Users Symposium, Turbomachinery Laboratory, Texas A&M University, 2010.

[11] F. E. Trevisan, M. Prado, Experimental investigation of the viscous effect on two-phase-flow patterns and hydraulic performance of electrical submersible pumps, Journal of Canadian Petroleum Technology 50 (04) (2011) 45–52.

[12] W. Monte Verde, J. L. Biazussi, N. A. Sassim, A. C. Bannwart, Experimental study of gas-liquid two-phase flow patterns within centrifugal pumps impellers, Experimental Thermal and Fluid Science 85 (2017) 37–51.

[13] C. Shao, C. Li, J. Zhou, Experimental investigation of flow patterns and external performance of a centrifugal pump that transports gas-liquid two-phase mixtures, International Journal of Heat and Fluid Flow 71 (2018) 460–469.

[14] L. Zhao, Z. Chang, Z. Zhang, R. Huang, D. He, Visualization of gas-liquid flow pattern in a centrifugal pump impeller and its influence on the pump performance, Measurement: Sensors 13 (2021) 100033.

[15] H. Stel, E. M. Ofuchi, R. H. Sabino, F. C. Ancajima, D. Bertoldi, M. A. Marcelino Neto, R. E. Morales, Investigation of the motion of bubbles in a centrifugal pump impeller, Journal of Fluids Engineering 141 (3).

[16] J. M. Cubas, H. Stel, E. M. Ofuchi, M. A. M. Neto, R. E. Morales, Visualization of two-phase gas-liquid flow in a radial centrifugal pump with a vaned diffuser, Journal of Petroleum Science and Engineering 187 (2020) 106848.

[17] R. M. Perissinotto, W. Monte Verde, M. S. d. Castro, J. L. Biazussi, V. Estevam, A. C. Bannwart, Experimental investigation of oil drops behavior in dispersed oil-water two-phase flow within a centrifugal pump impeller, Experimental Thermal and Fluid Science 105 (2019) 11–26.

[18] R. M. Perissinotto, W. Monte Verde, C. E. Perles, J. L. Biazussi, M. S. d. Castro, A. C. Bannwart, Experimental analysis on the behavior of water drops dispersed in oil within a centrifugal pump impeller, Experimental Thermal and Fluid Science 112 (2020) 109969.

40

[19] R. F. L. Cerqueira, R. M. Perissinotto, W. Monte Verde, J. L. Biazussi, M. S. Castro, A. C. Bannwart, Development and assessment of a particle tracking velocimetry (ptv) measurement technique for the experimental investigation of oil drops behavior in dispersed oil-water two-phase flow within a centrifugal pump impeller, International Journal of Multiphase Flow, accepted for publication.

[20] J. P. Valdés, M. Asuaje, N. Ratkovich, Study of an esp's performance handling liquid-liquid flow and unstable ow emulsions part i: Experimental, Chemical Engineering Science 223 (2020) 115726.

[21] P. Schmitt, S. Sibirtsev, M. W. Hlawitschka, R. Styn, A. Jupke, H.-J. Bart, Droplet size distributions of liquid-liquid dispersions in centrifugal pumps, Chemie Ingenieur Technik 93 (1-2) (2021) 129–142.

[22] N. A. V. Bulgarelli, J. L. Biazussi, W. M. Verde, C. E. Perles, M. S. de Castro, A. C. Bannwart, Experimental investigation on the performance of electrical submersible pump (esp) operating with unstable water/oil emulsions, Journal of Petroleum Science and Engineering 197 (2021) 107900.

[23] N. A. V. Bulgarelli, J. L. Biazussi, W. M. Verde, C. E. Perles, M. S. de Castro, A. C. Bannwart, Relative viscosity model for oil/water stable emulsion flow within electrical submersible pumps, Chemical Engineering Science 245 (2021) 116827.

[24] N. A. V. Bulgarelli, J. L. Biazussi, W. M. Verde, C. E. Perles, M. S. de Castro, A. C. Bannwart, A novel criterion based on slip ratio to assess the flow behavior of w/o emulsions within centrifugal pumps, Chemical Engineering Science 247 (2022) 117050.

[25] N. Pedersen, P. S. Larsen, C. B. Jacobsen, Flow in a centrifugal pump impeller at design and off-design conditions—part i: particle image velocimetry (piv) and laser doppler velocimetry (ldv) measurements, J. Fluids Eng. 125 (1) (2003) 61–72.

[26] J. Keller, E. Blanco, R. Barrio, J. Parrondo, Piv measurements of the unsteady flow structures in a volute centrifugal pump at a high flow rate, Experiments in fluids 55 (10) (2014) 1–14.

[27] N. Zhang, B. Gao, Z. Li, D. Ni, Q. Jiang, Unsteady flow structure and its evolution in a low specific speed centrifugal pump measured by piv, Experimental thermal and fluid science 97 (2018) 133–144.

41

[28] X. Li, B. Chen, X. Luo, Z. Zhu, Effects of flow pattern on hydraulic performance and energy conversion characterisation in a centrifugal pump, Renewable Energy 151 (2020) 475–487.

[29] B. Shi, K. Zhou, J. Pan, X. Zhang, R. Ying, L. Wu, Y. Zhang, Piv test of the flow field of a centrifugal pump with four types of impeller blades, Journal of Mechanics 37 (2021) 192–204.

[30] X.-D. Liu, Z.-Q. Liu, Q. Zhong, Y.-j. Li, W. Yang, Experimental investigation of relative velocity field based on image rotation method in pump impeller, Flow Measurement and Instrumentation 82 (2021) 102061.

[31] B. Chen, X. Li, Z. Zhu, Investigations of energy distribution and loss characterization in a centrifugal impeller through piv experiment, Ocean Engineering 247 (2022) 110773.

[32] N. Krause, E. Pap, D. Thévenin, Investigation of off-design conditions in a radial pump by using time-resolved-piv, in: Proceedings of the 13th International Symposium on Applications of Laser Techniques to Fluid Mechanics, Citeseer, 2006, pp. 1–11.

[33] S. Mittag, M. Gabi, Experimental investigation on pump-intake-elbow systems using refraction index matching and tr-spiv, in: 16th International Symposium on Transport Phenomena and Dynamics of Rotating Machinery, 2016.

[34] R. M. Perissinotto, W. D. P. Fonseca, R. F. L. Cerqueira, W. Monte Verde, J. L. Biazussi, M. S. Castro, A. C. Bannwart, Development of a transparent pump prototype for flow visualization purposes, in: Proceedings of Rio Oil & Gas Expo and Conference, Brazilian Petroleum and Gas Institute, 2022.

[35] A. J. Stepanoff, Centrifugal and axial flow pumps: theory, design, and application, Wiley, 1957.

[36] H. Petermann, C. Pfleiderer, Strömungsmaschinen, Springer, 1964.

[37] F. Scarano, M. L. Riethmuller, Iterative multigrid approach in piv image processing with discrete window offset, Experiments in Fluids 26 (6) (1999) 513–523.

[38] J. Keller, Estructuras de flujo y fluctuaciones fluidodinámicas en bombas centrífugas por interacción rotor-estator, doctoral thesis, Universidad de Oviedo, 2014.

[39] X. Li, H. Chen, B. Chen, X. Luo, B. Yang, Z. Zhu, Investigation of flow pattern and hydraulic performance of a centrifugal pump impeller through the piv method, Renewable Energy 162 (2020) 561–574.

[40] R. L. Burden, J. D. Faires, A. M. Burden, Numerical analysis, Cengage learning, 2015.

760 [41] R. M. Perissinotto, R. F. L. Cerqueira, W. Monte Verde, J. L. Biazussi, A. C. Bannwart, M. S. Castro, Visualization of oil-water emulsion formation in a centrifugal pump stage, in: 51st Turbomachinery and 38th Pump Symposia, Texas AM University, 2022.